Direct Analysis of Ore-Precipitating Fluids

Combined IR Microscopy and LA-ICP-MS Study of Fluid Inclusions in Opaque Ore Minerals

This is the Green open Access version of: Kouzmanov, K., Pettke, T. and Heinrich, C.A., 2010. Direct analysis of ore-precipitating fluids: combined IR microscopy and LA-ICP-MS study of fluid inclusions in opaque ore minerals. *Economic Geology*, vol. 105, pp. 351-373.
Original publication see: https://doi.org/10.2113/gsecongeo.105.2.351

Direct analysis of ore-precipitating fluids: combined IR microscopy and LA-ICP-MS study of fluid inclusions in opaque ore minerals

Kalin Kouzmanov[1,2*], Thomas Pettke[1] & Christoph A. Heinrich[1]**

[1]*Department of Earth Sciences, ETH Zurich, Clausiusstrasse 25, 8092 Zürich, Switzerland.*
[2]*Department of Mineralogy, University of Geneva, Rue des Maraîchers 13, 1205 Geneva, Switzerland.*
**corresponding author:*
e-mail: kalin.kouzmanov@unige.ch
Fax: +41 22 379 32 10
Phone: +41 22 379 68 93
***Present address: Institute of Geological Sciences, University of Bern, Baltzerstrasse 1+3, 3012 Bern, Switzerland.*

Keywords: LA-ICP-MS, near-infrared microscopy, fluid inclusions, enargite, pyrite, epithermal

Abstract

Laser-ablation inductively coupled plasma mass-spectrometry (LA-ICP-MS) in combination with near infrared microscopy of fluid inclusions hosted by ore minerals that are opaque to visible light can provide the composition of ore-precipitating fluids. We applied the two techniques to well constrained fluid inclusion assemblages hosted by pyrite, enargite and quartz, to trace the source and evolution of the fluids in high-sulfidation epithermal veins overprinting a porphyry copper deposit at Rosia Poieni, Romania. Despite some analytical limitations caused by the sulfide host minerals, the data demonstrate that fluids trapped in apparently cogenetic quartz and ore minerals are chemically different.

Systematic changes in major and trace element ratios between liquid-vapor, vapor-rich and brine fluid inclusion assemblages in the three minerals record an evolving fluid source at the porphyry to epithermal transition. Regarding their Cs/(Na+K) ratios, most of epithermal quartz-hosted fluid inclusion assemblages form a well-defined cluster, which coincides with the narrow range of the porphyry-stage fluids trapped in early quartz of the porphyry stockwork veins. Their Cu/(Na+K) ratios are 10-100 times lower compared to the pyrite-hosted inclusions and correspond to the lowest Cu/(Na+K) ratios recorded for the porphyry-stage fluids. By contrast, pyrite-hosted vapor-rich fluid inclusions have the highest Cu/(Na+K) similar to the highest Cu/(Na+K) ratios measured in the porphyry-stage fluid inclusions. The results lead to the conclusion that the gangue and ore minerals in the high-sulfidation epithermal veins at Rosia Poieni formed by successive pulses of chemically distinct hydrothermal fluids, which were successively exsolved from residual melt batches of a progressively crystallizing magma at greater depth. These results are consistent with detailed textural observations, but petrography alone could not have led to this unambiguous conclusion.

1. Introduction

Fluid inclusions in hydrothermal ore deposits are unique samples of paleo-hydrothermal fluids responsible for ore-formation, and are trapped within crystals of gangue as well as ore minerals (Roedder, 1984). As most of the metallic ore minerals are opaque to visible light fluid inclusions are commonly studied only in transparent gangue minerals, such as silicates (mainly quartz), sulfates, fluorite and carbonates. Interpretation of the P-T-X conditions of ore deposition then assumes that information obtained from gangue minerals is applicable to ore minerals, and in some cases this can be unambiguously demonstrated by careful petrography (e.g., Audétat et al., 1998) assisted by

cathodoluminescence imaging (e.g., Wilkinson et al., 1999; Rusk and Reed, 2002; Redmond et al., 2004; Landtwing et al., 2005). In other cases, this assumption is based on the close spatial association of gangue and ore minerals alone, even when their contemporaneous deposition cannot be demonstrated by unambiguous textural evidence.

Some pioneering studies of Edwin Roedder and co-workers in the 1960's, using the nowadays "classical" microthermometry technique (Roedder, 1962, 1963), the quantitative bulk analysis of alkalies (Roedder, 1958; Roedder et al., 1963) or ore metals in primary inclusion fluids (Czamanske et al., 1963), paved the way towards a more quantitative understanding of fluid processes related to ore-formation. These early studies motivated the development of a number of microanalytical techniques for bulk or *in situ* analysis of individual fluid inclusions in the last 20 years.

Near-infrared (NIR) transmitted-light microscopy is a powerful technique for observing internal structures of some ore minerals that are opaque to visible light (Campbell et al., 1984; Richards and Kerrich, 1993). Campbell and Robinson-Cook (1987) demonstrated the application of this technique to study fluid inclusions in such minerals in combination with microthermometric measurement. Since these pioneering papers, studies of fluid inclusions in different opaque minerals, including wolframite, enargite, stibnite, pyrite and other minerals have been performed (e.g., Campbell et al., 1988; Mancano and Campbell, 1995; Lüders 1996; Lüders and Ziemann, 1999; Bailly et al., 2002; Kouzmanov et al., 2002; Lindaas et al., 2002). Recently Moritz (2006) reported that temperatures of phase changes measured using NIR microthermometry of opaque minerals should be interpreted cautiously because they can vary with the IR light source intensity, resulting in a possible underestimation of homogenization temperatures and overestimation of fluid salinities. Despite these limitations, NIR microscopy is an effective tool for revealing growth textures in opaque minerals, and for comparing petrographic characteristics of fluid inclusion populations in coexisting transparent gangue and opaque ore minerals.

Since the late 1990s, laser-ablation inductively-coupled-plasma mass-spectrometry (LA-ICP-MS) has become a powerful and efficient multi-element microanalytical technique to quantify the composition of fluid inclusions trapped in minerals (Audétat et al., 1998; Günther et al., 1998; Loucks and Mavrogenes, 1999; Heinrich et al., 2003; Allan et al., 2005). Used in combination with microthermometric data, LA-ICP-MS provides important information on the concentrations of metals in hydrothermal fluids and mechanisms of ore deposition in hydrothermal systems (e.g., Audétat et al., 2000; Ulrich et al., 2001; Rusk et al., 2004; Landtwing et al., 2005; Klemm et al., 2007, 2008). Most LA-ICP-MS analyses of fluid inclusions were conducted on quartz samples with well constrained textural relationships with the ore minerals, allowing analyses of the chemistry of pre-, syn- and post-ore deposition fluids and their evolution with time. Recently Stoffell et al. (2008) and Wilkinson et al. (2009) reported LA-ICP-MS analyses of sphalerite-hosted fluid inclusions from Mississippi Valley-Type zinc-lead deposits, demonstrating that ore minerals in these systems precipitated from chemically distinct anomalously metal-rich batches of fluid compared to those precipitating the gangue minerals, suggesting some episodicity and potentially short duration of ore-forming pulses in hydrothermal systems. Similarly, Pettke and Frey (1996) reported Pb isotope disequilibrium between ore-forming fluids trapped in native gold and associated hydrothermal vein quartz from the Alps, suggesting that the fluid crystallizing free gold preserved clear indication of interaction with metamorphosed igneous rocks from the ocean floor that was not obvious from the quartz-hosted fluid inclusions.

In this contribution we describe the successful microanalysis of fluids directly depositing ore minerals, by combining the NIR microscopy technique and the LA-ICP-MS to quantify the concentrations of major and trace elements in single primary fluid inclusions trapped in ore minerals that are opaque to visible light (pyrite and enargite). Textural observations on the different quartz, pyrite and enargite generations in high-sulfidation epithermal veins crosscutting a porphyry Cu-Au system at Rosia Poieni (Romania) are linked with these analyses, to reconstruct the evolution of fluids at the porphyry to epithermal transition.

2. Geologic setting of the Rosia-Poieni porphyry Cu-Au deposit

The Rosia Poieni porphyry Cu-Au deposit (431 Mt of ore at 0.55% Cu and 0.25 g/t Au; Kouzmanov et al. 2005a) is located in the northern sector of the South Apuseni Mountains in Western Romania, and belongs to the historically most important gold district in Europe, known as the "Golden Quadrilateral" (Udubasa et al., 2001). The district hosts numerous spatially associated porphyry Cu-(Au) and

epithermal Au-Ag deposits related to Miocene magmatic activity (Bostinescu 1984; André-Mayer et al., 2001; Ciobanu et al., 2004; Milu et al., 2004; Rosu et al., 2004). Previous studies in this district have indicated a dominantly magmatic signature for the mineralizing fluids in the low- to intermediate-sulfidation epithermal Au-Ag deposits, mainly based on stable isotope data (Alderton and Fallick, 2000) or a combination of stable isotopes and fluid inclusion chemistry (LA-ICP-MS data; Wallier et al., 2006).

The Rosia Poieni deposit, located 4 km to the NE of the diatreme-hosted epithermal Au-Ag deposit of Rosia Montana (Manske et al., 2006; Wallier et al., 2006), shows all of the characteristics of a classical porphyry copper system. The Poieni diorite porphyry, intruding Cretaceous sedimentary rocks, constitutes the main intrusion of the magmatic stock hosting the porphyry Cu-Au deposit. Minor mafic (biotite-phyric) and aplitic dikes cut the Poieni diorite. The intrusive stock is overlain by the Rotunda andesite composed of domes, thick lava flows and pyroclastic breccias. The U-Pb dates of magmatic zircons from the earliest mineralized Poieni diorite porphyry (9.42-9.23 Ma) and a synmineralization dike (9.16 Ma) constrain the late Miocene age of mineralization (Kouzmanov et al., 2005b), several million years later than Rosia Montana. Classical zonation of the alteration associated with the porphyry Cu mineralization was recognized, where potassic, phyllic, advanced argillic, and propylitic alteration zones were developed from the deep central part of the intrusion towards shallower and distal portions (Milu et al., 2004). The porphyry mineralization occurs in the central potassic alteration zone and comprises a dense network of veins and veinlets containing characteristic purple quartz and variable amounts of magnetite, chalcopyrite, pyrite and minor bornite, chalcocite and molybdenite. The porphyry system is overprinted by intense advanced-argillic alteration and high-sulfidation epithermal veining along discrete fracture zones (Fig. 1; Kouzmanov et al., 2004; Milu et al., 2004), as described in the next section. The transition from porphyry to epithermal environment of ore formation coincided with vigorous fluid-assisted brecciation of the host rocks and the formation of breccia and pebble dikes (Fig. 1a). These structures were the main channels that focused the mineralizing fluids and have the same orientation, alteration and mineralization patterns as the high-sulfidation quartz-pyrite-enargite veins (Fig. 1b; Kouzmanov et al., 2004). The high-sulfidation veins have haloes of vuggy silica and advanced-argillic alteration (Fig. 1c), and are in turn cut by later polymetallic quartz-sphalerite-galena veins associated with zones of phyllic alteration.

Previous fluid inclusion studies of quartz stockwork veins at Rosia Poieni using microthermometry, Raman microspectrometry, SEM and PIXE (Damman et al., 1996) and LA-ICP-MS (Pettke et al., 2001) indicate that the fluids of the early porphyry stage were trapped in the two-phase field characterized by co-existing vapor-rich (1-5 wt% NaCl equiv.) and brines (up to 67 wt% NaCl equiv.). Damman et al. (1996) defined successive episodes of phase separation in the porphyry veins, based on microthermometric results and the microchemistry of the fluids and qualitatively documented very high Cu contents of the vapor-rich inclusions. Pettke et al. (2001) reported relative enrichment of As and Sb, and, to a lesser extent, Cu in the vapor phase, whereas Na, K, Rb, Cs, Pb, Zn and Fe are preferentially enriched in the brine. Nedelcu et al. (2001) identified complex chloride "inclusions" in sulfide minerals from several porphyry Cu and epithermal Au deposits in the South Apuseni Mountains, studied by SEM and EDS analysis, indicating that fluid inclusions were also formed in ore minerals in the porphyry and epithermal veins.

3. High-sulfidation epithermal veining at Rosia Poieni

Fracture zones with a dense network of epithermal veins and associated alteration overprint the potassic and phyllic alteration zones in the eastern part of the present day open pit at Rosia Poieni. Up to 30 cm wide, almost vertical NNW-SSE trending breccia and pebble dikes are the main mineralized structures. Vertical extent of these structures often exceeds 25 m and they can be followed on several levels in the open pit. Their matrix consists of fine-grained pyrite ± enargite, microcrystalline silica, alunite and rock flour. Rock fragments are altered to advanced argillic assemblage, consisting of quartz, alunite, diaspore and pyrophyllite. Fragments of porphyry-stage purple quartz veins are common. Subparallel to these structures and probably immediately following their formation, vertically extensive (>10 m), swarms of up to 5 cm wide quartz-pyrite-enargite veins are developed. Bulk grade of these veins ranges from 0.05 to 0.75 ppm Au and from 5 to 25 ppm Ag and can reach 2.5 % Cu, 0.43 % Zn and 0.05% Pb (6 ICP analyses). The zonation pattern of their alteration halos (Fig. 1c) – from vuggy silica to advanced argillic, argillic and phyllic alteration assemblages towards the host rock – is typical for high-sulfidation epithermal systems (Arribas, 1995).

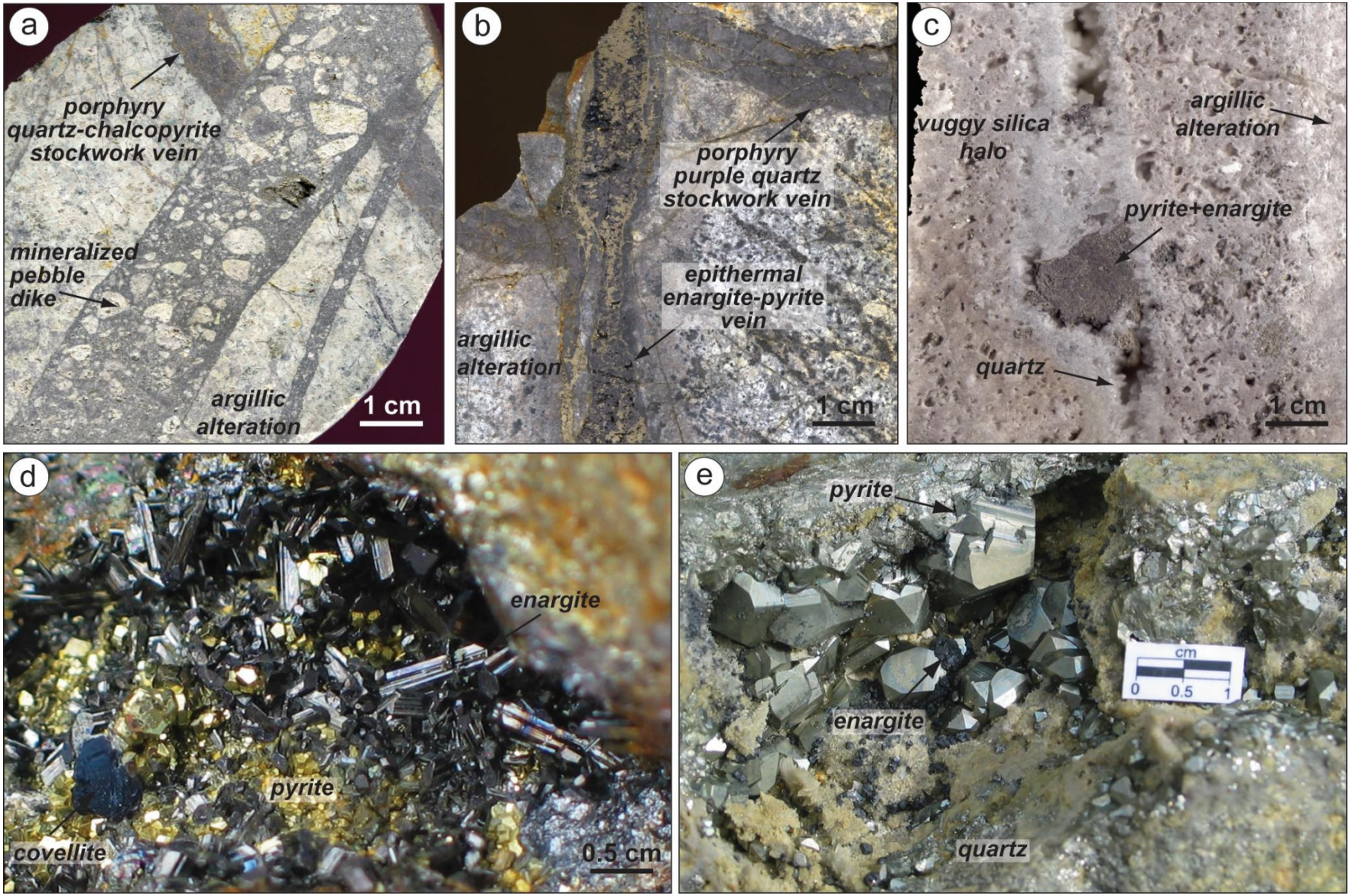

Figure 1. High-sulfidation epithermal veins at Rosia Poieni: **a**) Tiny mineralized pebble dike offsetting a porphyry quartz-chalcopyrite stockwork vein. Rock fragments are altered to advanced argillic assemblage; **b**) Thin enargite-pyrite high-sulfidation vein with argillic alteration halo offsetting a porphyry purple quartz stockwork vein; **c**) Typical zoning of the alteration halo along a high-sulfidation quartz-pyrite-enargite vein; **d**) Drusy texture of enargite indicating open space filling; e) Euhedral pyrite crystals overgrown by quartz and enargite in a vug.

Figure 2 summarizes the paragenetic sequence in the high-sulfidation epithermal veins at Rosia Poieni, based on detailed transmitted- and reflected-light microscopy, NIR microscopy, scanning-electron microscope-back-scattered-electron (SEM-BSE) observations, electron microprobe analysis (EPMA) and scanning-electron microscope-cathodoluminescence (SEM-CL) study. These veins are dominated by quartz and pyrite, but also include enargite, colusite, tennantite-goldfieldite, subordinate chalcopyrite, bornite, digenite and covellite, as well as various Au-, Au-Ag, Bi-, and Au-Bi tellurides and sulfotellurides. Such an assemblage is indicative of a high- to very high sulfidation state of the mineralizing fluids (Einaudi et al., 2003).

Textural relationships between alteration and ore minerals clearly indicate intense leaching of the host rock by extremely acidic fluids prior to sulfide precipitation. According to their textural, alteration and ore mineralogy patterns, the high-sulfidation veins at Rosia Poieni have all of the characteristics of high-sulfidation epithermal ore deposits (Arribas, 1995; Sillitoe and Hedenquist, 2003).

The present fluid inclusion study is focused on these high-sulfidation epithermal veins crosscutting the porphyry system at Rosia Poieni and more specifically on the two main opaque minerals constituting these veins – pyrite and enargite. The samples investigated come mainly from epithermal veins showing druzy textures resulting from open space filling (Fig. 1d), or large cavities and vugs formed in the Poieni diorite (Fig. 1e) resulting from intense leaching of the rock.

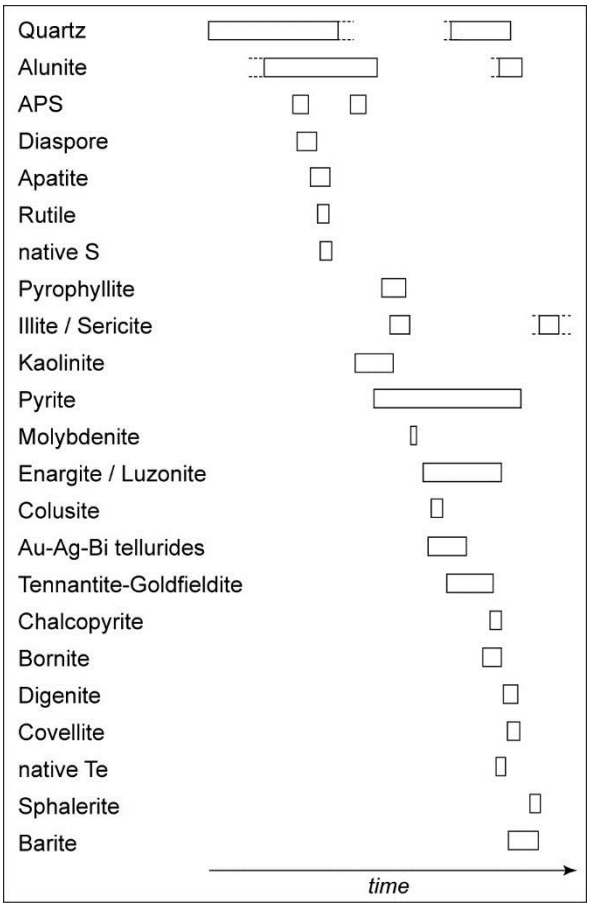

Figure 2. Paragenetic sequence of the high-sulfidation veins.

4. Sample preparation and analytical approach

Single crystals of pyrite and enargite were extracted from veins with clear textural relationships between the different minerals and prepared as doubly polished oriented crystal mounts (100-150 μm in thickness), cut parallel to the cubic (100) or octahedral (111) faces of the pyrite and to the prismatic (100) or (210) faces of the enargite. Pyrite crystals (5-15 mm in size; Fig. 1e) are euhedral, bounded mainly by the most common {100}, {111} and {210} forms; in addition, small faces of {112} and two other {hkl} forms were identified. Enargite crystals (5-10 mm long; Fig. 1d) have prismatic morphology, shaped mainly by {100}, {001}, {101}, {110} and {210}.

NIR petrography was carried out at the University of Geneva on an Olympus BH2-MA microscope equipped with an infrared Hamamatsu C2400 tube-type camera which allows IR observations up to 2500 nm (Lüders 1996). Limited microthermometric measurements on enargite-hosted fluid inclusions were done using a U.S.G.S. gas-flow heating/freezing system, while quartz-hosted fluid inclusions were studied using a Linkam microthermometric stage. Synflinc standards (Sterner and Bodnar, 1984) were measured for calibration using the IR equipment and also in normal transmitted light.

LA-ICP-MS analyses were conducted on a 193 nm ArF Excimer laser with an energy homogenized beam profile coupled with an ELAN 6100 DRC ICP quadrupole mass spectrometer (QMS) at ETH Zurich (Günther et al., 1997, 1998; Heinrich et al. 2003). Table 1 provides a summary of the analytical conditions and data acquisition parameters used for LA-ICP-MS analyses. The ablation rate for pyrite and enargite was between 0.1 and 0.2 μm/pulse. The optical imaging system permits precise visual positioning of ablation points and the use of different pit diameters (8-100 μm) at constant energy density on the sample, by adjusting an aperture in the laser beam path. The fluid inclusions in pyrite and enargite were ablated with a constant diameter of the laser beam, while for quartz-hosted inclusions a stepwise increase of the beam diameter was used (Günther et al. 1998). The sample was loaded along with the SRM 610 glass NIST standard in a 1 cm^3 ablation cell on a modified Zeiss petrographic microscope. Laser ablation aerosol was transferred to the ICP-QMS by a mixed He-Ar carrier gas. Analyses of a maximum of 16 unknowns were bracketed by measurement of the external SRM 610 standard to correct for drift by linear regression. Concentrations of up to 18 elements were measured in each fluid inclusion (Table 1). Quantification of single-inclusion LA-ICP-MS signal involves the integration of each element, background subtraction, host mineral correction for the signal, and comparison of signal intensities with the external standard. The absolute elemental concentrations are derived by comparison of elemental ratios to independent estimates of fluid inclusion salinity, derived from microthermometry and expressed in wt. % NaCl equiv., including a correction for salinity contributions from other major salts in the fluid inclusions (K, Mn, Fe, Zn and Pb chlorides; Heinrich et al. 2003).

Electron microprobe analyses (EPMA) of pyrite and enargite were performed to identify the stoichiometry of the two minerals and to select an element to be used as an internal standard for the LA-ICP-MS analyses. EPMA and X-ray elemental mapping were carried out using a Jeol JXA 8200 Superprobe WD/ED combined microanalyzer at the University of Lausanne. Accelerating voltage of 15 kV, beam current of 20 nA, and beam diameter of 1 μm were used. Standards used were as follows: FeS_2 (Fe-*K*□, S-*K*□), GaAs (As-*L*□), Sb_2S_3 (Sb-*L*□), Cu metal (Cu-*K*□), ZnS (Zn-*K*□), MnS (Mn-*K*□), Te metal (Te-*L*□), Bi_2Se_3 (Bi-*M*□, Se-*L*□), Ag metal (Ag-*L*□). Counting times of 20 s on the peak and 10 s on the background on both sides of the peak were used for major elements; counting times for trace elements were 40s and 20s, respectively.

5. Near-infrared (NIR) microscopy

5.1. Pyrite-hosted fluid inclusions

Pyrite crystals appear homogeneous in reflected-light microscopy, back-scattered electron (BSE) images (Fig. 3a) and X-ray elemental mapping. However, the NIR petrography revealed the presence of three distinct generations of pyrite (Fig. 3b): *pyrite-1* is homogeneous in NIR light and without mineral inclusions except quartz and alunite; *pyrite-2* is characterized by oscillatory zoning in NIR light and the presence of numerous solid (enargite, bornite and chalcopyrite) and fluid inclusions, trapped along growth zones (Fig. 3a-c); *pyrite-3* is completely opaque in NIR light and occurs as a tiny rim (200-300 μm) overgrowing *pyrite-2*, hosting small prismatic inclusions of covellite. No trace elements are present in concentrations higher than the detection limit of the electron microprobe (300-400 ppm, using the given analytical conditions) in any of the three pyrite generations.

Figure 4a summarizes the fluid inclusions types in the different pyrite, quartz and enargite generations and their relative timing of entrapment. The two generations of pyrite that are transparent to NIR radiation host different types of fluid inclusions. *Pyrite-1* hosts the same types of fluid inclusions as *quartz-1* (Figs. 4b-c): three-phase liquid-vapor-halite inclusions and vapor-rich inclusions occurring as separate pseudosecondary trails. These two types of fluid inclusions do not coexist and do not form typical "boiling" assemblages. They were trapped as two distinct types of fluids in the earliest generations of quartz and pyrite. L-V-halite inclusions with similar volumetric proportions between the three phases have been also observed as late secondary trails in porphyry

Table 1. LA-ICP-MS machine and data acquisition parameters

Excimer 193 nm ArF laser Compex 110I	**Pyrite**	**Enargite**	**Quartz**
Output energy	30 mJ	20 mJ	30-50 mJ
Homogeneous energy density on sample	10-15 J/cm^2	<5 J/cm^2	10-15 J/cm^2
Pulse duration	15 ns	15 ns	15 ns
Repetition rate	10 Hz	10 Hz	10 Hz
Pit sizes	30-60 µm	30-75 µm	30-40 µm
Ablation cell	In-house built plexiglass chamber with anti-reflection coated silica glass window		
Cell He gas flow	1.0 l/min He	1.0 l/min He	1.0 l/min He
ELAN 6100 quadrupol ICP-MS			
Nebulizer gas flow	0.85-0.87 l/min Ar	0.80 l/min Ar	0.86 l/min Ar
Auxiliary gas flow	0.75 l/min Ar	0.80 l/min Ar	0.80 l/min Ar
Cool gas flow	14,0 l/min Ar	14,0 l/min Ar	14,0 l/min Ar
rf-power	1350 kV	1300 kV	1400 kV
Detector mode	Dual	Dual	Dual
Quadrupole setting time	3 ms	3 ms	3 ms
Data acquisition parameters			
Sweeps per reading	1	1	1
Readings per replicate	400-500	300-450	320-550
Replicates	1	1	1
Dwell time per isotope	40 ms for Au, 20 ms for Cu, As and Ag 10 ms for all others	40 ms for Au, 20 ms for Fe, Ag, Sb, Te 10 ms for all others	10 ms for all elements
Points per peak	1 per measurement	1 per measurement	1 per measurement
Oxide production rate	tuned to <0.5 % ThO	tuned to <0.5 % ThO	tuned to <0.5 % ThO
Isotopes analyzed	*Program "Fluid inclusions":* ^{7}Li, ^{23}Na, ^{29}Si, ^{39}K, ^{57}Fe, ^{65}Cu, ^{66}Zn, ^{75}As, ^{77}Se, ^{85}Rb, ^{88}Sr, ^{107}Ag, ^{121}Sb, ^{125}Te, ^{132}Cs, ^{136}Ba, ^{197}Au, ^{208}Pb *Program "Trace elements":* ^{57}Fe, ^{59}Co, ^{62}Ni, ^{65}Cu, ^{66}Zn, ^{75}As, ^{77}Se, ^{95}Mo, ^{107}Ag, ^{118}Sn, ^{121}Sb, ^{125}Te, ^{197}Au, ^{205}Tl, ^{208}Pb, ^{209}Bi	*Program "Fluid inclusions":* ^{23}Na, ^{39}K, ^{55}Mn, ^{57}Fe, ^{65}Cu, ^{66}Zn, ^{75}As, ^{77}Se, ^{85}Rb, ^{88}Sr, ^{107}Ag, ^{121}Sb, ^{125}Te, ^{132}Cs, ^{136}Ba, ^{197}Au, ^{208}Pb, ^{209}Bi	*Program "Fluid inclusions":* ^{7}Li, ^{23}Na, ^{29}S, ^{39}K, ^{55}Mn, ^{57}Fe, ^{65}Cu, ^{66}Zn, ^{75}As, ^{77}Se, ^{85}Rb, ^{88}Sr, ^{107}Ag, ^{125}Te, ^{132}Cs, ^{136}Ba, ^{197}Au, ^{208}Pb, ^{209}Bi

stockwork vein-stage quartz crystals. *Pyrite-2* contains exceptionally large (up to several millimeters) primary fluid inclusion cavities (Kouzmanov et al., 2007). In doubly polished sections these can be seen as open cavities formed along growth zones (Fig. 3a-c, e). Sometimes, smaller channel-like and elongated inclusions are preserved, forming typical boiling assemblages of two-phase liquid-vapor and coexisting vapor-rich inclusions trapped in the same growth zones of *pyrite-2* (Fig. 4e). Similar boiling assemblages have been also observed as secondary trails in *quartz-1* and *quartz-2* (Fig. 4d).

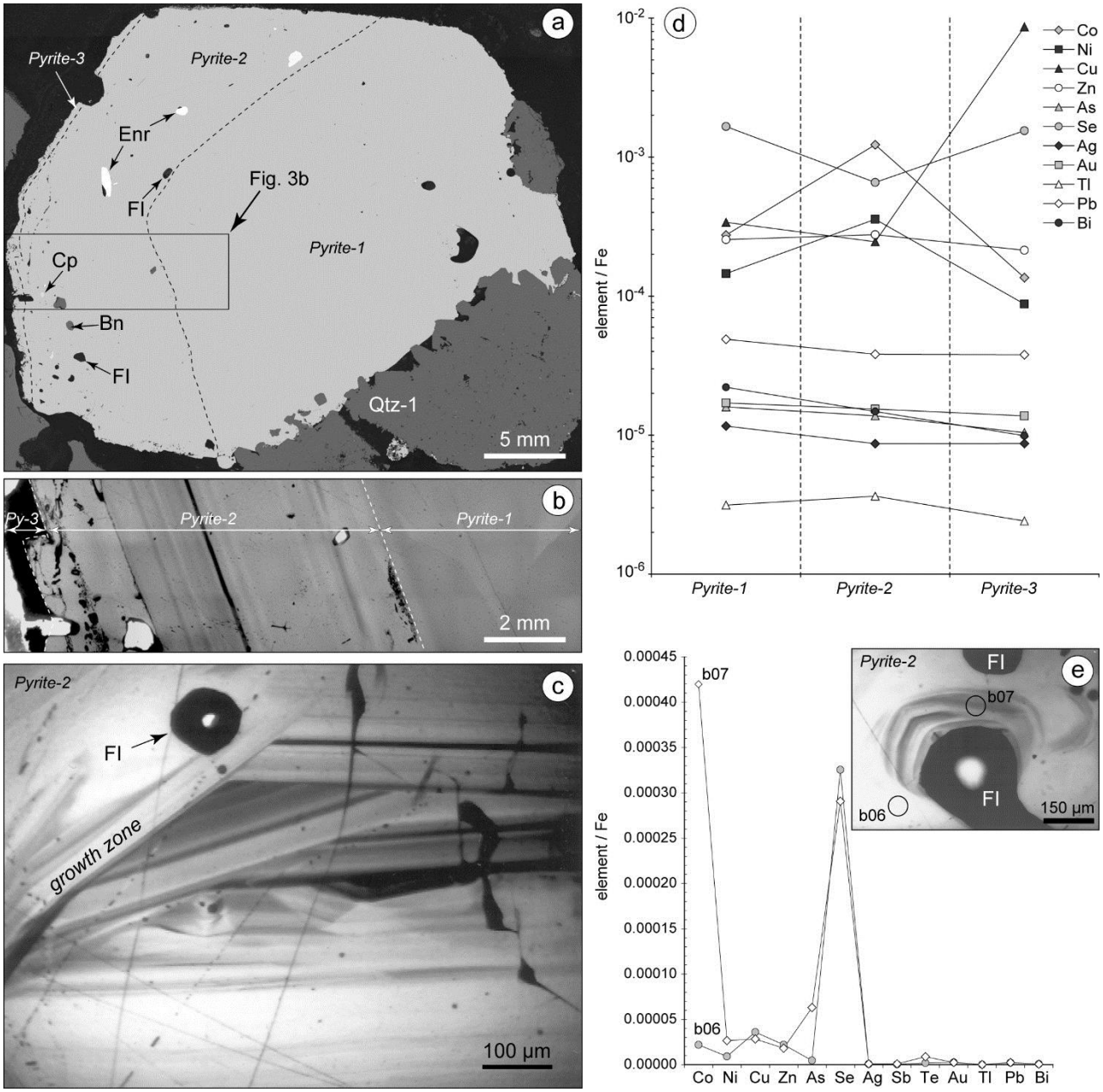

Figure 3. Textures and compositions of different pyrite generations in high-sulfidation veins: **a)** Distribution of three pyrite generations within a single crystal (BSE image), defined based on NIR petrography (see Figure 3b and text for discussion). Note the abundance of fluid inclusion cavities and enargite, bornite and chalcopyrite inclusions in *pyrite-2*; **b)** NIR composite microphotograph showing the three generations of pyrite: homogeneous *pyrite-1*, *pyrite-2* marked by oscillatory growth zoning and numerous fluid and solid inclusions and *pyrite-3* which is completely opaque to the NIR radiation; **c)** Complex crystal zoning of *pyrite-2* resulting from variable Co content (NIR transmitted light microphotograph). Large fluid inclusion cavity was formed parallel to a growth zone; **d)** Average composition of the three pyrite generations expressed in metal/Fe ratios based on LA-ICP-MS analyses; **e)** LA-ICP-MS analyses (metal/Fe ratios) of dark and bright zones in *pyrite-2* clearly indicate that Co is the trace-element causing the IR zonation of this pyrite generation. Growth zoning around very large fluid inclusion cavity in *pyrite-2* is a common phenomenon (see the NIR transmitted light microphotograph). Location of the ablation pits of the analyses b06 and b07 is also shown. *Abbreviations:* Bn = bornite, Cp = chalcopyrite, Enr = enargite, FI = exposed to the surface fluid inclusion cavity, Qtz = quartz.

Microthermometric measurements have not been performed on pyrite-hosted fluid inclusions, because of the analytical problems related to the incident IR light intensity as discussed by Moritz (2006). The three-phase brine inclusions trapped in *quartz-1* and as secondary trails in the porphyry quartz have salinities in the narrow range 34-36 wt% NaCl equiv and homogenization temperatures ranging from 293° to 340°C. The salinity of the two-phase liquid-vapor inclusions from boiling assemblages in *quartz-2* ranges between 0.9 and 1.2 wt% NaCl equiv; temperatures of homogenization vary between 250° and 284°C. Other liquid-vapor only fluid inclusion assemblages in *quartz-1* have salinities as high as 10-11 wt% NaCl equiv.

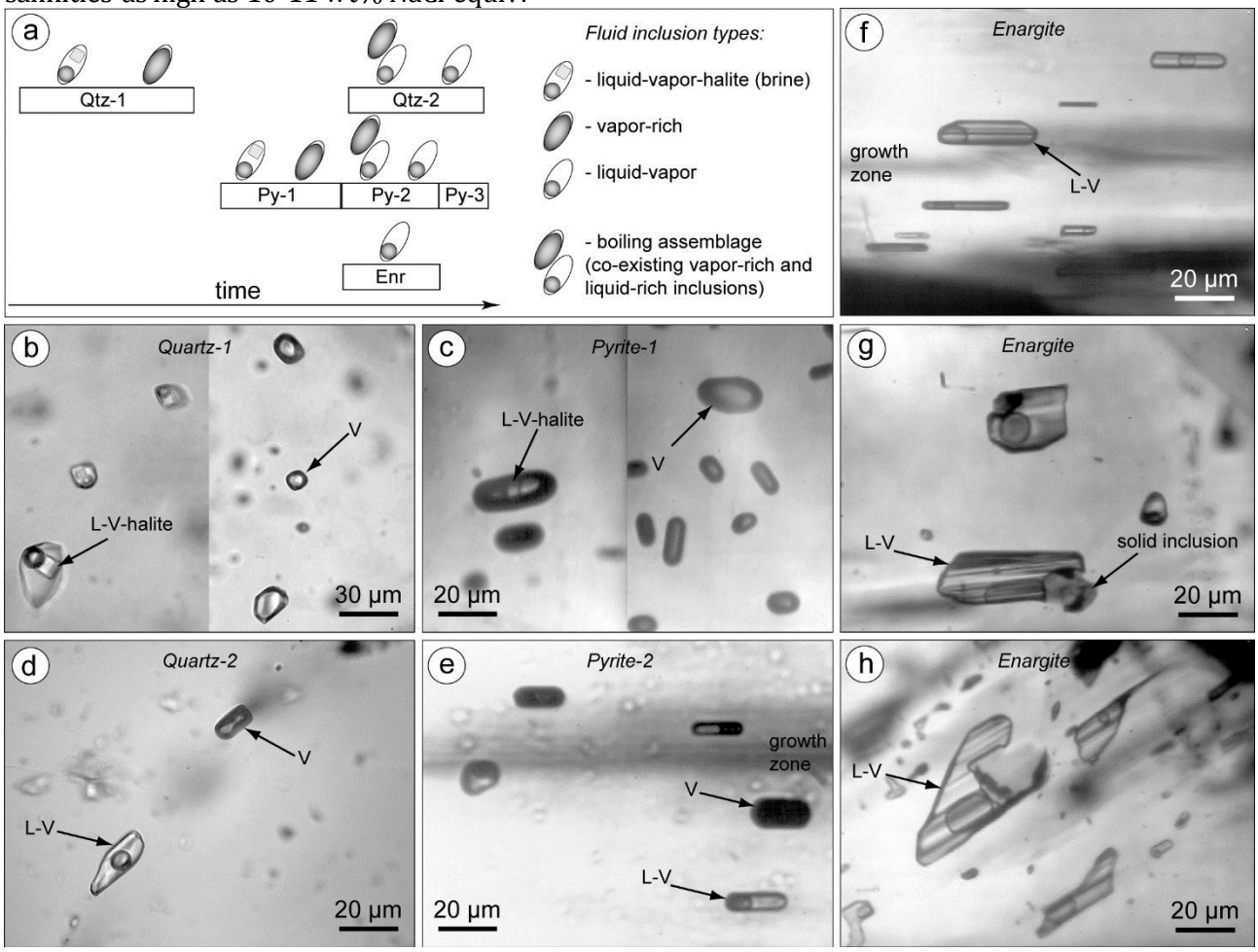

Figure 4. Types of fluid inclusions in quartz, pyrite and enargite from high-sulfidation epithermal veins: **a)** Graphical summary of the inclusion types trapped in different generations of quartz, pyrite and enargite as primary or pseudosecondary fluid inclusion assemblages; **b-c)** Pseudosecondary L-V-halite and vapor-rich inclusion trails in *quartz-1* and *pyrite-1*. The two fluid inclusion types do not form boiling assemblages and belong to different fluid generations. They were observed only in the early generations of pyrite and quartz; **d)** Pseudosecondary trail of coexisting liquid-rich and vapor-rich inclusions, forming boiling assemblage in *quartz-2*; **e)** Primary coexisting liquid-rich and vapor-rich inclusions trapped along a growth zone in *pyrite-2*; **f)** Primary liquid-rich inclusions parallel to a growth zone in enargite; **g)** Primary liquid-rich fluid inclusions attached to solids trapped in growth zones of enargite; **h)** Typical secondary fluid inclusion assemblage in enargite, resulting of leakage. Note the different L/V ratio in the inclusions. *Abbreviations:* Enr = enargite; L = liquid; Py = pyrite, Qtz = quartz, V = vapor.

5.2. Enargite-hosted fluid inclusions

Enargite occurs as inclusions in *pyrite-2* (Fig. 3a) and also as free-grown prismatic crystals in vugs (Fig. 1d). In NIR transmitted light, enargite often displays complex oscillatory and/or sector zoning (Fig. 5a). BSE images and X-ray elemental mapping (Fig. 5b-c) do not show any correlation between the IR transmittance of the enargite and the distribution of a single trace element. However, the observed BSE image zonation correlates well with the Sb distribution, as revealed by the X-ray map (Fig. 5c). Electron microprobe analyses reveal relatively constant composition of the enargite, Sb being the only trace element systematically detectable in the range 0.3-0.8 wt%. Random analyses show Te and Bi concentrations as high as 0.11 and 0.20 wt%, respectively.

In enargite only two-phase liquid-vapor inclusions have been observed: as typical primary assemblages along growth zones (Fig. 4f), or as cavities "attached" to solid inclusions (Fig. 4g). Most

primary inclusions in enargite are flat, tabular to channel-like, rarely isometric or with striated faces. The liquid/vapor ratio in these inclusions is very constant and is similar to the liquid/vapor ratio observed in the pyrite-hosted two-phase inclusions (Fig. 4e). Secondary fluid inclusion assemblages with highly variable liquid/vapor ratios, due to leakage, are also present in enargite (Fig. 4h). In the following analytical study, only primary fluid inclusions in enargite were taken into consideration.

Moritz (2006) used one of the primary enargite-hosted fluid inclusions from our samples to do the tests on the accuracy of the IR microthermometry as a function of the light intensity. He obtained a salinity of 1.05 wt% NaCl equiv and a temperature of homogenization of 317°C for this inclusion, using the lowest possible light intensity. Salinities of two other inclusions were measured later using the same method and they were 0.88 and 1.05 wt% NaCl equiv.

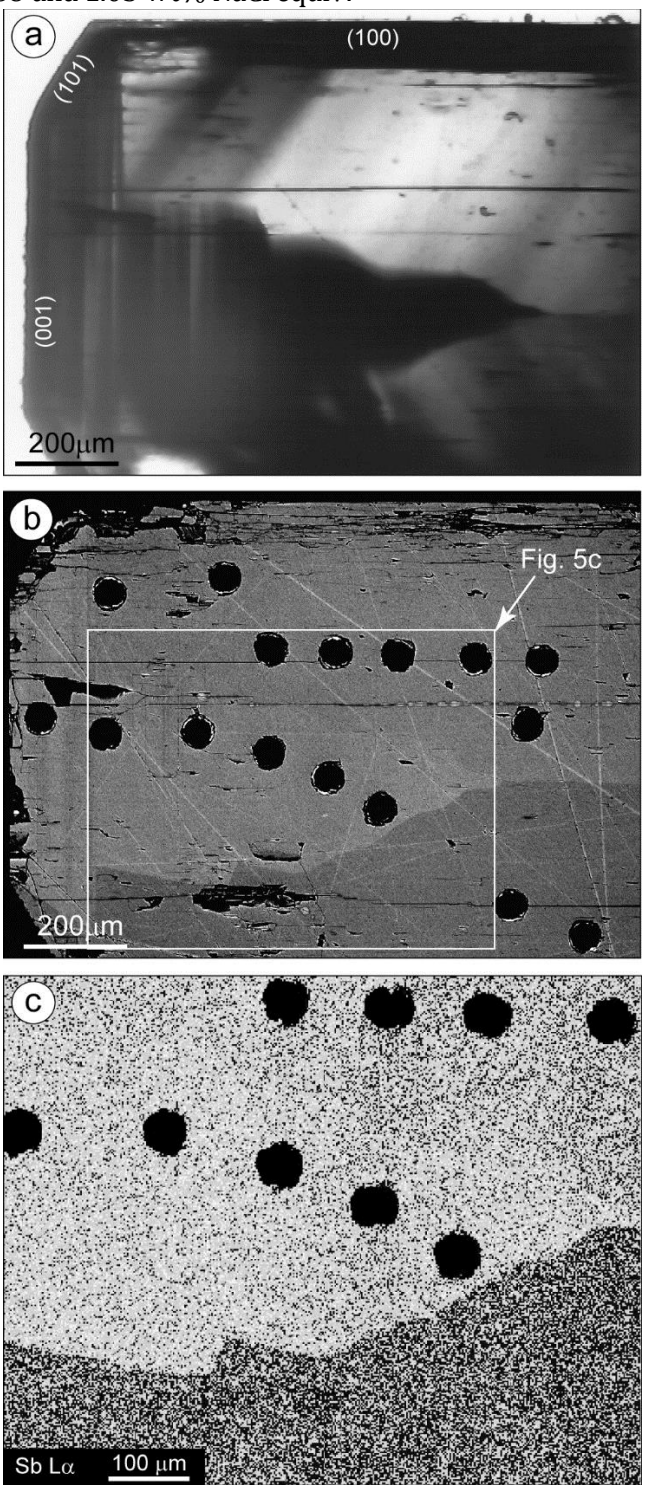

Figure 5. Textural and compositional features of zoned single enargite crystal from a high-sulfidation vein, cut parallel to (100): **a)** Complex sector zoning formed by (001), (101) and (100) sectors (NIR transmitted light microphotograph); **b)** BSE image of the crystal from Figure 5a; **c)** Antimony distribution in the central part of the enargite crystal (X-ray element map).

6. LA-ICP-MS results

6.1. Sulfide host

LA-ICP-MS analyses of pyrite were performed to determine the nature of its NIR zonation and to evaluate the trace-element content of the host mineral for subsequent separation of fluid inclusion contributions to mixed LA-ICP-MS signals. All analyses were carried out with an ablation pit diameter of 60 μm (Table 1). Ablation tests were conducted prior to analyses in order to achieve an ablation rate of ~0.1-0.15 μm/pulse.

Figure 6 shows SEM images of ablation craters produced in pyrite and enargite. Ablation pits in pyrite are well defined, with sharp rims and relatively flat bottoms (Fig. 6a); no melting features are observed. Despite efforts to minimize the effect of melting, melting did occur during the ablation of enargite, resulting in the formation of tiny spherical melt droplets and larger elongated globules in the ablation pit and the surrounding area (Fig. 6b).

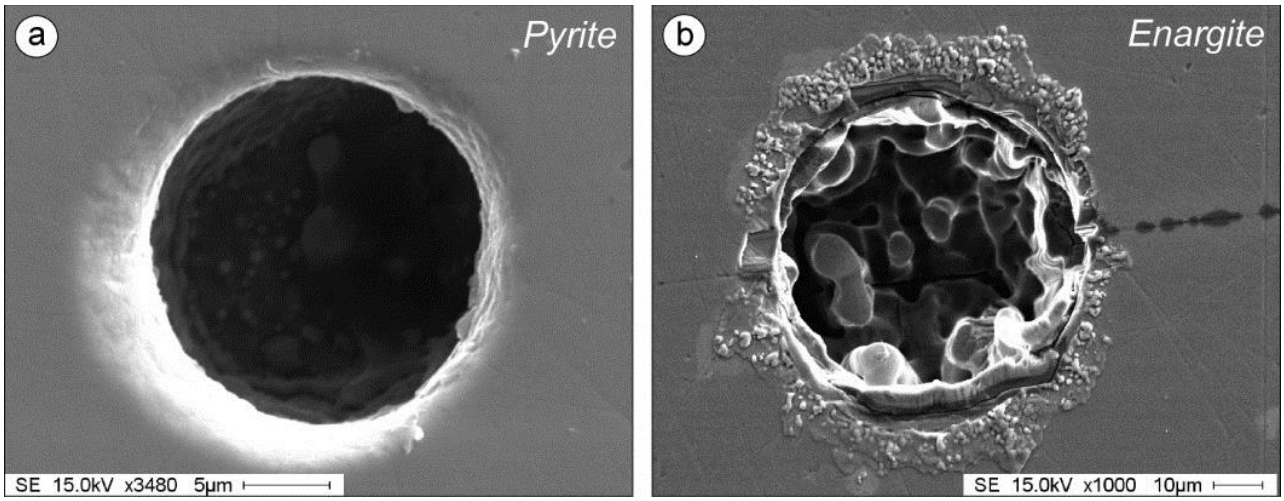

Figure 6. Scanning electron microscope (SEM) images of laser-ablation pits in pyrite (**a**) and enargite (**b**). Note the globular textures in the ablation pit in enargite, testifying to melting that occurred during laser ablation.

Typical transient signals for selected elements obtained from the ablation of pyrite and enargite are shown in Figure 7a-b. No evidence of time-related element fractionation can be seen on the transient signal. However, fractionation cannot be excluded, resulting from the melting that occurs during ablation and potential element partitioning between the solid, melt and plasma formed during this melting process (e.g., Watling et al., 1995; Watling 1998).

Table 2 summarizes the results of the LA-ICP-MS analyses of pyrite. For quantification we used the stoichiometric value of 46.55 wt% Fe as an internal standard, because no other major or trace elements were detected during the electron microprobe analyses of pyrite. The three texturally different generations of pyrite exhibit distinct trace-element content (Fig. 3d; Table 2). Metal/Fe ratios are used for the plots in order to better visualize chemical zonation patterns. Cobalt and Ni are enriched in *pyrite-2*, while Se is depleted in this generation. The highest Se values were detected in *pyrite-1*. Copper is more abundant in *pyrite-3* than in the first two generations. These elevated values could be due to incorporation of Cu into the pyrite structure (e.g. Pačevski et al., 2008), as well as to the presence of microinclusions of covellite identified also as larger grains. All other trace elements have relatively constant concentrations in the three pyrite generations.

In order to understand the nature of the strong oscillatory zoning of *pyrite-2* seen in NIR transmitted light (Fig. 3c), LA-ICP-MS analyses in transparent and dark zones were performed (Fig. 3e), indicating that Co controls this variation. In the opaque zones of *pyrite-2* the Co content ranges between 140 and 400 ppm. This was also noted by Kulis and Campbell (1999) who reported theoretical calculations suggesting that IR-zonation in pyrite is most likely caused by crystal-field transitions of low-spin Co^{2+} ions, which occur in a $Fe_{(1-x)}Co_xS_2$ solid solution as stoichiometric substitutions for Fe^{2+}. The IR opacity of *pyrite-3* is most probably due to the high Cu content (usually few hundreds of ppm).

In pyrite, Ag and Au have been detected in concentrations higher than the limit of detection (LOD). Silver content ranges from 0.6 to 1.7 ppm, and Au ranges from 1.0 to 2.3 ppm (Table 2). The three pyrite generations have relatively constant content of Ag and Au, which correlate positively with each other.

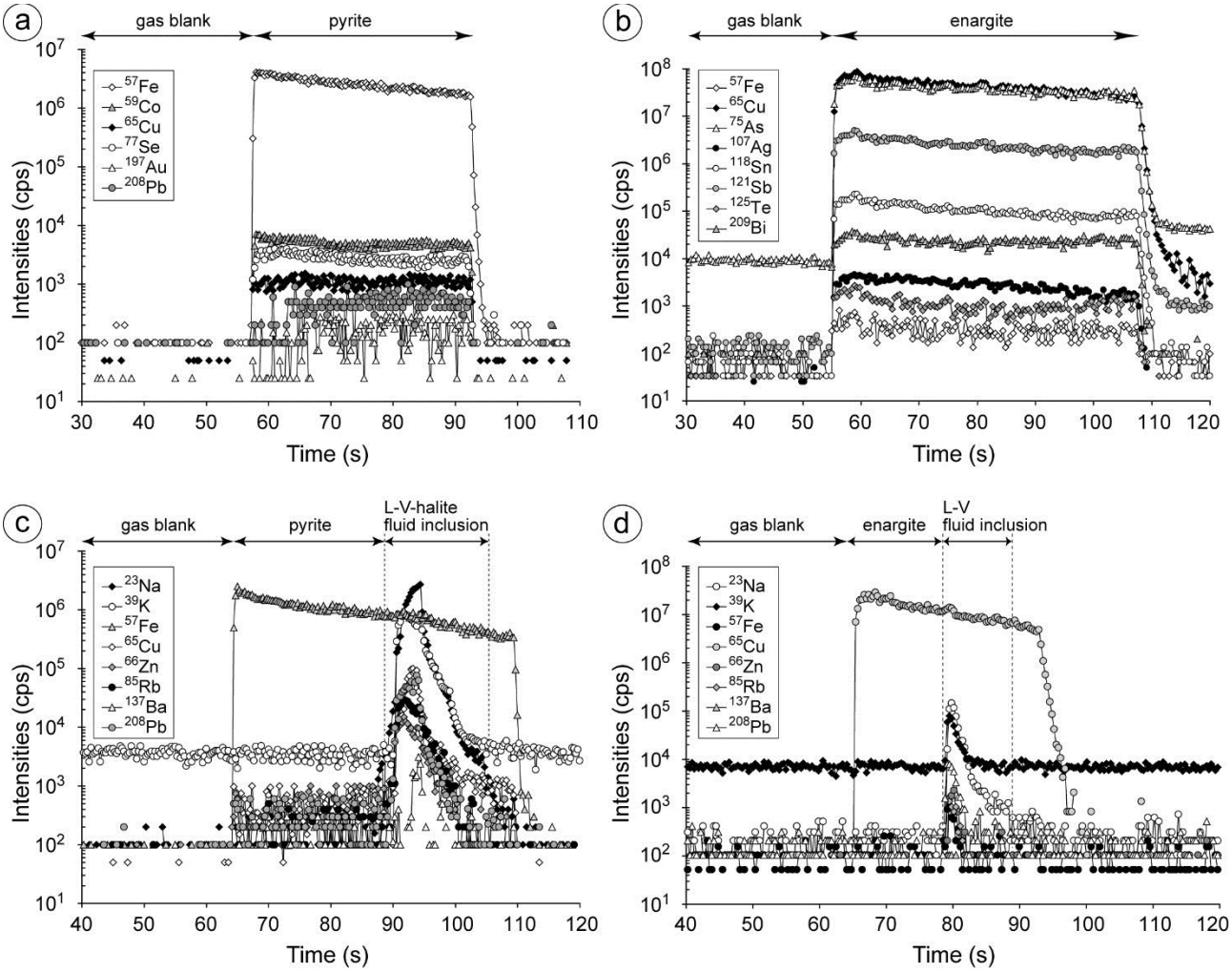

Figure 7. Typical transient signals for selected elements obtained from the ablation of pyrite **(a)**, enargite **(b)**, pyrite-hosted L-V-halite fluid inclusion **(c)**, and enargite-hosted L-V fluid inclusion **(d)**, after spike elimination. Gas background composition is shown as the first segment of the spectra.

Table 2. Element Concentrations of Selected Trace Elements in Pyrite from a High-Sulfidation Epithermal Vein (LA-ICP-MS analyses)

N°	Analysis	Pyrite generation	Co (ppm)	Ni (ppm)	Cu (ppm)	Zn (ppm)	As (ppm)	Se (ppm)	Mo (ppm)	Ag (ppm)	Sn (ppm)	Sb (ppm)	Te (ppm)	Au (ppm)	Tl (ppm)	Pb (ppm)	Bi (ppm)
1	my04d03	Pyrite-1	26	11	27	17	2,3	146	1,9	1,7	1,8	1,2	1,9	1,4	0,26	6,9	4,3
2	my04d04	Pyrite-1	26	15	32	23	1,5	142	1,5	1,1	1,8	1,4	2,0	2,0	0,40	5,1	1,9
3	my04d05	Pyrite-1	22	17	35	33	1,4	160	1,8	1,2	1,8	1,3	1,5	1,4	0,35	4,4	2,1
4	my04d06	Pyrite-1	15	11	50	28	1,1	231	2,1	0,9	1,5	1,2	0,6	2,2	0,30	4,3	1,4
5	my04d07	Pyrite-1	48	19	26	27	1,7	152	1,2	0,8	1,9	1,3	1,0	1,5	0,26	3,9	1,4
		Pyrite-1	*28*	*15*	*34*	*26*	*1,6*	*166*	*1,7*	*1,2*	*1,8*	*1,3*	*1,4*	*1,7*	*0,31*	*4,9*	*2,2*
6	my04e03	Pyrite-2	143	70	24	24	1,6	88	1,0	0,9	1,8	1,4	1,0	1,5	0,29	3,2	1,5
7	my04e04	Pyrite-2	26	25	26	31	1,5	63	1,4	0,8	1,8	1,3	0,9	1,6	0,51	3,6	1,1
8	my04e05	Pyrite-2	27	25	30	33	1,4	60	1,1	0,8	1,4	1,6	1,5	1,6	0,49	3,8	1,8
9	my04e06	Pyrite-2	37	20	25	25	1,2	68	1,1	1,0	1,5	1,3	1,2	1,8	0,31	4,6	1,9
10	my04e07	Pyrite-2	381	39	19	25	1,2	50	1,4	0,9	1,5	1,1	1,3	1,2	0,23	4,0	1,2
		Pyrite-2	*123*	*36*	*25*	*28*	*1,4*	*66*	*1,2*	*0,9*	*1,6*	*1,3*	*1,2*	*1,5*	*0,36*	*3,8*	*1,5*
11	my04e08	Pyrite-3	3,6	7,9	957	26	1,6	208	1,1	1,5	2,2	1,0	0,9	2,3	0,21	4,5	1,3
12	my04e09	Pyrite-3	7,8	9,2	216	20	0,8	84	1,6	0,9	1,7	1,1	1,3	1,4	0,30	4,6	1,1
13	my04e10	Pyrite-3	59	18	34	19	0,9	55	0,8	0,6	1,3	0,9	1,4	1,2	0,20	3,2	0,7
14	my04e11	Pyrite-3	3,7	6,2	1005	27	1,2	125	1,2	0,8	1,6	1,3	0,9	1,4	0,22	4,4	1,1
15	my04e12	Pyrite-3	5,3	6,2	596	14	0,8	111	0,9	0,8	1,5	0,7	0,9	1,0	0,25	3,2	0,7
16	my04e13	Pyrite-3	2,7	5,0	2382	22	0,9	347	1,3	0,6	1,3	0,8	2,8	1,0	0,28	2,8	1,0
		Pyrite-3	*13,6*	*8,8*	*865*	*21*	*1,0*	*155*	*1,2*	*0,9*	*1,6*	*1,0*	*1,4*	*1,4*	*0,24*	*3,8*	*1,0*

Note: Stoichiometric Fe content of 46.55 wt% has been used for internal standardization of LA-ICP-MS.
Average concentrations for the three generations of pyrite are shown *in italic*.

6.2. NIR mapping of pyrite- and enargite-hosted fluid inclusions

In order to allow for "blind shooting" on the laser with its visible-light-only setup (no NIR camera is attached to our laser system), and to guarantee precise and complete ablation of the total volume of each individual fluid inclusion, careful mapping of all fluid inclusion assemblages in NIR transmitted and combined transmitted/reflected light has been done prior to analysis (Fig. 8). During the analytical sessions positioning of the ablation crater was chosen based only on the reflected light image obtained on the Zeiss microscope through which the sample is viewed in the LA-ICP-MS cell. Therefore, fluid inclusions images taken in combined NIR transmitted and visible reflected light focused on the sample surface were crucial for the success of this study (Fig. 8b). Then, the exact location of the ablation pit and its diameter has been adjusted based on the geometry of different irregularities on the polished surface of the sample (such as scratches and holes) and the fluid inclusion size.

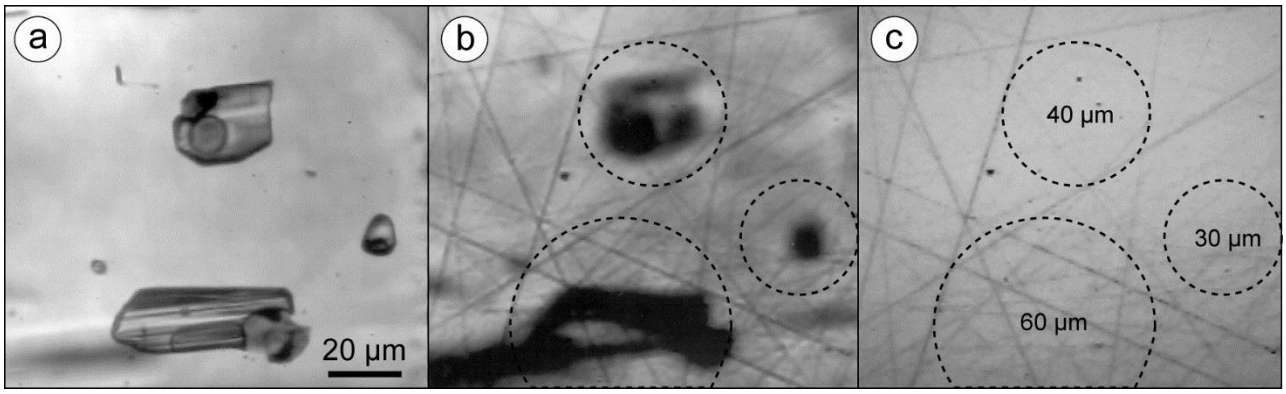

Figure 8. NIR light petrography mapping used for the LA-ICP-MS analyses. Detailed mapping of fluid inclusion assemblages hosted by pyrite and enargite in NIR transmitted, transmitted / reflected and visible reflected light allowed precise positioning of the ablation pit using only the reflected light image on the Zeiss microscope: **a)** NIR microphotograph in transmitted light focused on fluid inclusion assemblage situated at depth of about 30 µm from the polished surface of the sample; **b)** NIR microphotograph in transmitted / reflected light focused on the sample surface; **c)** Reflected light microphotograph of the same locality.

6.3. Fluid inclusions

Figures 7c and 7d illustrate time-resolved signals resulting from the ablation of pyrite-hosted liquid-vapor-halite and enargite-hosted liquid-vapor fluid inclusions, respectively. Each analysis started with monitoring the gas background for ~60 s (first segment of the spectra). The first section of the ablation signal, until the fluid inclusion is ablated, corresponds to pure host mineral. The second section of the ablation signal corresponds to a simultaneous analysis of mixed material from the host and the fluid inclusion itself. In addition to alkalies, some metals are clearly enriched in the fluid inclusions, compared to the host (e.g., Cu, Zn and Pb – in pyrite and Fe, Zn, Pb – in enargite). After the entire inclusion is ablated, resulting in a smooth decrease of the element intensities back to background values, the last section of the ablation signal corresponds again to pure host mineral.

Because of potential problems with internal inclusion heating during IR microthermometry (Moritz, 2006), only a very limited number of microthermometric measurements on enargite-hosted inclusions were performed at very low illumination intensity, indicating salinities very close to 1 wt% NaCl equiv. This salinity overlaps the more abundant salinity data from some texturally-related quartz-hosted fluid inclusions. Thus, the salinity estimates for pyrite- and enargite-hosted inclusions, used as internal standards for LA-ICP-MS analyses, were taken as average values of 35, 1 and 0.5 wt. % NaCl equiv for the liquid-vapor-halite, liquid-vapor and vapor-rich fluid inclusions, respectively.

Analytical results for 63 pyrite-hosted, 21 enargite-hosted and 19 quartz-hosted fluid inclusions from the high-sulfidation epithermal veins are reported in Table 3. In total, 19 fluid inclusion assemblages, consisting of 2 to 10 single fluid inclusions, were analyzed: 6 liquid-vapor-halite "brine" assemblages, 3 vapor-rich assemblages and 10 two-phase liquid-vapor assemblages. Low-salinity inclusions in pyrite have lower elemental concentrations and higher detection limits (based on the 3□ criterion of the background for each element) than for brine inclusions of comparable size. Element concentrations in vapor-rich inclusions are commonly below or near the limit of detection. For some inclusions, concentrations of elements such as As, Sb, Te, Au, Ag, are orders of magnitude higher than the average for the assemblage, indicating probably heterogeneous entrapment of solid phases together with the hydrothermal fluid.

Table 3. LA-ICP-MS Analyses of Pyrite-, Enargite- and Quartz-Hosted Fluid Inclusions from High-Sulfidation Epithermal Veins, Rosia Poieni Porphyry Cu-Au Deposit, Romania

N°	FI assem	Analysis	Host mineral	Type of FI	Abl. pit, µm	Li, ppm	Na, ppm	Si, ppm	K, ppm	Mn, ppm	Fe, ppm	Cu, ppm	Zn, ppm	As, ppm	Se, ppm	Rb, ppm	Sr, ppm	Ag, ppm	Sb, ppm	Te, ppm	Cs, ppm	Ba, ppm	Au, ppm	Pb, ppm	Bi, ppm
1	A01	my04b0303	Pyrite-1	brine	50	388	111628	6561	28165	n.a.	mx	3009	29240	52	<13	447	42	<0.3	2,1	71	83	173	<0.4	13251	n.a.
2	A01	my04b0404	Pyrite-1	brine	50	410	112692	<1751	25864	n.a.	mx	2761	28718	7,0	<21	438	84	<0.9	<1.7	39	76	140	<0.5	13300	n.a.
3	A01	my04b0505	Pyrite-1	brine	40	448	109324	2399	31125	n.a.	mx	3161	31545	30	118	472	62	<0.6	1,9	368	83	151	<0.3	14192	n.a.
4	A01	my04b0606	Pyrite-1	brine	30	383	115614	<10214	25033	n.a.	mx	3370	23792	28	608	375	61	<4.9	<6.9	58	111	105	6,5	11069	n.a.
5	A02	my04b0909	Pyrite-1	brine	40	260	117970	13187	21546	n.a.	mx	2571	20567	<6.9	<32	325	65	<1.6	12	246	66	166	3,8	12104	n.a.
6	A02	my04b1010	Pyrite-1	brine	40	707	117141	<23789	25320	n.a.	mx	1392	20818	<59	1892	459	185	<13	<23	475	188	41	16,1	9503	n.a.
7	A02	my04b1111	Pyrite-1	brine	30	288	118096	<29787	22211	n.a.	mx	2366	20364	<56	1912	361	61	<15	<33	240	70	4080	<7.6	11002	n.a.
8	A02	my04b1212	Pyrite-1	brine	30	<631	126933	<314912	22494	n.a.	mx	16441	4370	<830	13314	875	124	<132	453	<1339	146	<395	<64	2000	n.a.
9	A02	my04b1313	Pyrite-1	brine	40	489	119053	<2515	44469	n.a.	mx	13997	3845	10,2	<25	683	34	<1.1	<2.4	224	87	100	6,6	1453	n.a.
10	A02	my04b1414	Pyrite-1	brine	30	470	126294	84144	25062	n.a.	mx	10272	4176	<1244	<734	326	699	<25	<53	636	36	<66	41	1079	n.a.
11	A02	my04b1515	Pyrite-1	brine	40	382	116054	6954	24951	n.a.	mx	2102	22745	39	262	386	48	<1.4	<3.3	227	87	92	5,9	11145	n.a.
12	A02	my04b1616	Pyrite-1	brine	40	1163	108437	<12611	34615	n.a.	mx	8874	30565	<24	1308	519	103	<5.3	<11	367	104	151	<2.6	14115	n.a.
13	A02	my04b1717	Pyrite-1	brine	40	536	110684	12477	26693	n.a.	mx	3970	31198	78	263	437	60	<1.6	<1.8	41	113	109	3,6	15865	n.a.
14	A02	my04b1818	Pyrite-1	brine	40	964	129053	85153	8669	n.a.	mx	1516	9976	<33	392	181	72	96	63	254	69	66	14,2	4890	n.a.
15	A03	my04c0303	Pyrite-1	brine	30	237	113825	<8266	27916	n.a.	mx	2621	24544	32	<74	418	22	<3.1	<8	106	88	80	<1.9	12579	n.a.
16	A03	my04c0404	Pyrite-1	brine	30	1211	115400	<25572	25999	n.a.	mx	1487	19633	171	<345	331	88	<10	<25	<188	105	70	<6.8	16947	n.a.
17	A03	my04c0505	Pyrite-1	brine	30	469	113836	<5353	27444	n.a.	mx	3170	25023	23	<58	435	50	<2.6	<3.3	<29	79	52	6,9	12461	n.a.
18	A03	my04c0606	Pyrite-1	brine	30	262	117696	<7227	24045	n.a.	mx	2019	22070	101	<92	366	<1.9	<3.3	<7.4	<58	56	<4.7	<2	7277	n.a.
19	A03	my04c0707	Pyrite-1	brine	30	190	120260	<19338	21141	n.a.	mx	2314	16677	<43	<251	342	259	56	105	<127	68	24	31	10056	n.a.
20	A03	my04c0808	Pyrite-1	brine	30	204	118632	<29588	22816	n.a.	mx	1860	18853	190	558	350	53	<19	<27	<214	101	161	<12	10462	n.a.
21	A03	my04c1010	Pyrite-1	brine	30	<208	119786	<67584	14034	n.a.	mx	<108	13816	<163	<718	92	<8.8	<21	<52	3718	<16	<51	<21	26325	n.a.

22	A03	my04c1111		Pyrite-1	brine	30	354	122163	<12918	14602	n.a.	mx	1885	17538	<31	<137	343	57	7,6	<9.9	273	77	<10	<4	10794	n.a.
23	A03	my04c1212		Pyrite-1	brine	40	438	119590	<9217	16067	n.a.	mx	1317	21814	<26	<123	210	30	<3.3	<7.3	629	80	<11	<2.9	11815	n.a.
24	A03	my04c1313		Pyrite-1	brine	40	626	115808	<14491	20549	n.a.	mx	1057	25452	48	<192	313	26	<5.2	<12	357	102	<18	<4.7	14115	n.a.
25	A04	jl13b03	03	Pyrite-1	brine	40	489	105602	<2823	29737	n.a.	mx	1748	39610	81	650	465	45	7,8	12	484	114	62	32	17722	n.a.
26	A04	jl13b05	05	Pyrite-1	brine	40	524	97573	<1287	45357	n.a.	mx	2581	43213	57	75	695	16	2,5	4,1	179	117	17	2,5	20343	n.a.
27	A04	jl13b06	06	Pyrite-1	brine	40	453	107373	<1792	27642	n.a.	mx	2986	35954	88	140	409	42	7,2	9,4	574	92	89	4,0	19660	n.a.
28	A04	jl13b07	07	Pyrite-1	brine	40	613	108885	<2016	24971	n.a.	mx	3725	34765	84	258	383	65	4,9	4,2	589	84	112	2,4	19574	n.a.
29	A04	jl13b08	08	Pyrite-1	brine	40	734	109691	<1541	23727	n.a.	mx	5232	34364	87	267	425	58	7,3	8,4	430	90	143	6,9	18912	n.a.
30	A04	jl13b09	09	Pyrite-1	brine	40	391	105348	<2264	37370	n.a.	mx	5147	33324	80	<31	512	103	8,2	15	283	94	260	8,9	17606	n.a.
31	A05	jl12b03	03	Pyrite-1	V	30	10,2	1675	<2147	780	n.a.	mx	<3.9	<7.1	<5.4	37	<0.7	4,6	<0.9	<2.5	<12	<0.3	<2.1	<0.5	<1.3	n.a.
32	A05	jl12b04	04	Pyrite-1	V	30	<7.8	1642	<2168	830	n.a.	mx	30	31	<5.6	349	2,5	0,7	<0.9	<2.9	<16	0,7	<1.6	<0.8	1,7	n.a.
33	A05	jl12b05	05	Pyrite-1	V	30	<2.2	1957	<997	<18	n.a.	mx	<2.1	24	<2.3	<13	<0.2	<0.2	<0.4	4,7	1472	<0.1	<0.7	<0.3	<0.6	n.a.
34	A05	jl12b06	06	Pyrite-1	V	30	2,7	1821	<488	385	n.a.	mx	<1	3,5	3,8	59	<0.2	<0.1	<0.2	0,9	<3	<0.1	<0.2	<0.2	<0.4	n.a.
35	A05	jl12b07	07	Pyrite-1	V	30	2,2	1961	<218	15	n.a.	mx	47	<0.7	<0.4	7,4	0,4	0,6	0,2	0,7	11	0,2	<0.1	<0.1	0,5	n.a.
36	A05	jl12b08	08	Pyrite-1	V	40	7,4	1935	<182	40	n.a.	mx	1332	33	<0.4	4,4	9,5	0,4	1,1	1,5	<1.1	9,1	3,9	0,5	13	n.a.
37	A05	jl12b09	09	Pyrite-1	V	40	<0.3	1963	<147	11	n.a.	mx	67	<0.5	<0.3	<1.7	<0.1	0,4	<0.1	<0.1	2,9	<0.1	<0.1	<0.04	<0.1	n.a.
38	A06	jl13a03	03	Pyrite-1	V	40	32,7	1567	<1721	379	n.a.	mx	<2.3	531	<4.7	<25	5,4	1,4	1,7	<1.9	1479	1,1	2,0	5,2	153	n.a.
39	A06	jl13a04	04	Pyrite-1	V	40	5,6	1941	<341	26	n.a.	mx	<0.5	40	3,7	<4.9	0,2	0,3	0,8	0,4	<2	0,3	0,9	0,4	0,7	n.a.
40	A06	jl13a05	05	Pyrite-1	V	40	355,4	785	<1693	2922	n.a.	mx	<2.5	211	9,2	<22	12,9	11	7,7	3,3	<9.1	2,3	21	3,2	<1.1	n.a.
41	A06	jl13a06	06	Pyrite-1	V	40	38,1	1664	<1744	597	n.a.	mx	<2.5	172	<4.4	<20	3,1	0,2	1,0	<1.8	<5.4	<0.2	<1.6	2,8	33	n.a.
42	A06	jl13a07	07	Pyrite-1	V	40	123,7	1386	<10909	1397	n.a.	mx	<16	134	<28	<123	5,8	8,1	33	<9.5	<34	<1.2	31	<3.2	9,3	n.a.
43	A06	jl13a08	08	Pyrite-1	V	40	491,5	1617	<5635	<99	n.a.	mx	<9.6	809	<16	<72	10,4	<1.1	18	<7.2	<32	5,9	<7.2	5,7	23	n.a.
44	A06	jl13a09	09	Pyrite-1	V	40	25,1	1952	<1537	<23	n.a.	mx	<2.9	28	7,3	<19	2,7	<0.3	3,8	<1.9	469	0,9	<1.9	2,2	<1.1	n.a.
45	A06	jl13a10	10	Pyrite-1	V	40	<1	1014	<418	2540	n.a.	mx	<0.7	<1.8	<1.1	<5.9	1,4	<0.1	<0.2	<0.5	1,8	0,0	<0.3	<0.1	<0.3	n.a.
46	A06	jl13a11	11	Pyrite-1	V	40	<2	1870	<838	256	n.a.	mx	<0.9	<2.9	<2.1	<8.9	<0.2	0,7	<0.3	<0.9	939	<0.1	<0.8	1,6	1,4	n.a.
47	A06	jl13a12	12	Pyrite-1	V	40	<1.7	1936	<611	76	n.a.	mx	<1.1	4,1	1,4	<8.4	<0.1	0,2	<0.3	0,6	<3.3	0,2	<0.3	<0.2	1,5	n.a.
48	A06	jl13a13	13	Pyrite-1	V	40	<28.3	1967	<9214	<155	n.a.	mx	<37	<45	<24	<131	<2.3	<1.1	<3.5	<11	3420	<1.5	61	<4.6	<6.1	n.a.
49	A06	jl13a14	14	Pyrite-1	V	40	<1.7	1226	<579	1937	n.a.	mx	<1.3	27	<1.5	<7.8	1,0	<0.1	<0.1	0,9	940	<0.1	<0.4	<0.3	15	n.a.
50	A06	jl13a16	16	Pyrite-1	V	40	<26	1816	<10918	398	n.a.	mx	<20	<48	<28	<159	<3.1	<2.7	<2.2	<12	<67	<1.2	<13	<3.2	<8.6	n.a.
51	A07	jl13b10	10	Pyrite-1	V	40	<14.8	1581	<5265	944	n.a.	mx	113	76	<13	801	1,7	1,4	<1.3	<5.7	<32	1,3	<2.7	10,9	3,8	n.a.
52	A07	jl13b11	11	Pyrite-1	V	40	<5.8	1252	<2279	556	n.a.	mx	303	832	13,6	717	10,4	0,6	3,3	5,9	936	2,2	4,6	11,4	625	n.a.
53	A08	my04a0404		Pyrite-2	L-V	50	35	2606	429	2830	n.a.	mx	51	545	0,6	<1.3	24,5	4,6	0,8	<0.1	2,2	3,2	2,2	0,3	163	n.a.
54	A08	my04a0505		Pyrite-2	L-V	50	24	2586	<71	2885	n.a.	mx	51	542	1,0	<0.8	24,5	2,3	<0.1	<0.1	2,0	1,3	1,5	0,1	166	n.a.

55	A08	my04a0808		Pyrite-2	L-V	50	22	2371	<131	3378	n.a.	mx	58	608	<0.3	<1.1	23,9	2,8	0,1	<0.1	4,4	1,5	8,6	<0.1	179	n.a.
56	A08	my04a1212		Pyrite-2	L-V	40	57	2533	<1896	3069	n.a.	mx	74	506	<4.1	69	24,3	11	<0.9	<1.1	<8.8	5,3	2,4	3,4	162	n.a.
57	A09	jl12a03	03	Pyrite-2	L-V	40	70	2181	<122	3807	n.a.	mx	109	666	1,3	1,8	26,5	1,5	1,0	1,2	5,7	4,6	15	1,1	198	n.a.
58	A09	jl12a04	04	Pyrite-2	L-V	30	29	1903	286	4443	n.a.	mx	84	729	0,5	3,8	33,1	2,0	0,3	3,1	7,2	5,8	2,8	0,3	252	n.a.
59	A09	jl12a05	05	Pyrite-2	L-V	30	24	3001	<251	1916	n.a.	mx	37	450	<0.6	16	13,9	0,5	2,5	<0.3	1,2	1,4	2,4	0,2	112	n.a.
60	A09	jl12a06	06	Pyrite-2	L-V	40	11	2795	4272	2336	n.a.	mx	591	551	<1	55	18,4	1,1	3,4	<0.5	7,1	1,4	5,6	3,0	140	n.a.
61	A09	jl12a08	08	Pyrite-2	L-V	40	58	3200	<452	1460	n.a.	mx	299	402	<1.1	13	8,5	0,4	5,6	<0.5	<1.3	1,8	3,3	1,7	83	n.a.
62	A09	jl12a09	09	Pyrite-2	L-V	40	3,3	3431	6129	1104	n.a.	mx	177	174	<1.5	85	8,4	1,2	0,9	<0.8	<3.9	0,4	1,6	<0.2	67	n.a.
63	A09	jl12a10	10	Pyrite-2	L-V	40	<4.3	2731	<1254	2577	n.a.	mx	371	494	<3.1	147	11,0	<0.3	<0.6	<1.6	<8.3	1,3	7,6	<0.4	130	n.a.
64	B1	nm02a07		Enargite	L-V	40	n.a.	2659	n.a.	871	821	<3246	mx	380	mx	<536	17	<7.5	<12	mx	<105	<5.8	<28	<12	<50	<12
65	B1	nm02a08		Enargite	L-V	60	n.a.	2654	n.a.	683	2078	<2151	mx	215	mx	<430	<10.6	<6	<9.2	mx	<106	2,3	<19	<8	<36	<11
66	E1	nm02a09		Enargite	L-V	40	n.a.	2940	n.a.	1070	395	770	mx	56	mx	<66	9,1	5,0	<1.5	mx	<13	2,0	15	<1.4	185	4,5
67	A1	nm02a10		Enargite	L-V	40	n.a.	2790	n.a.	1252	394	976	mx	120	mx	<33	7,9	1,9	<1	mx	<6	1,0	9,2	<0.6	53	<0.9
68	A1	nm02a11*		Enargite	L-V	40	n.a.	2181	n.a.	1040	2961	<3197	mx	<189	mx	<611	<16.9	<8.7	<19	mx	<111	<2.4	<45	46	<61	<16
69	A1	nm02a12		Enargite	L-V	30	n.a.	2828	n.a.	1234	407	917	mx	85	mx	<64	9,7	2,0	<1.9	mx	<12	1,4	7,1	<1.1	65	1,4
70	A1	nm02a13		Enargite	L-V	30	n.a.	2767	n.a.	1194	391	999	mx	216	mx	<238	6,9	<2.6	<6.7	mx	<55	<1.8	11	<4.7	38	<4.9
71	A1	nm02a14		Enargite	L-V	30	n.a.	2726	n.a.	1328	378	1058	mx	145	mx	84	8,8	1,2	<1.7	mx	<14	1,0	6,1	<1.2	36	<1.4
72	A2	nm02b03		Enargite	L-V	30	n.a.	2605	n.a.	1291	432	1251	mx	155	mx	<57	28	3,6	21	mx	<14	1,2	19	<1	114	<1.2
73	A2	nm02b04		Enargite	L-V	30	n.a.	2840	n.a.	1200	456	836	mx	119	mx	<44	9,4	2,6	2,3	mx	<11	0,7	3,8	<0.8	71	1,7
74	A2	nm02b05		Enargite	L-V	30	n.a.	2904	n.a.	1222	428	678	mx	145	mx	<44	11	1,3	4,6	mx	<12	1,2	8,8	<0.9	67	1,2
75	A2	nm02b06		Enargite	L-V	30	n.a.	2399	n.a.	1301	385	1778	mx	138	mx	<303	7,7	3,7	12	mx	<86	3,0	<10	<6.3	99	<7.4
76	A2	nm02b07		Enargite	L-V	60	n.a.	2652	n.a.	1297	371	1309	mx	93	mx	<13	8,3	3,9	17	mx	<4.2	1,8	20	0,9	30	2,4
77	A2	nm02b08		Enargite	L-V	30	n.a.	2819	n.a.	1193	379	932	mx	135	mx	<61	16	4,1	12	mx	<15	1,5	8,4	<1	103	17
78	L1	nm02b11		Enargite	L-V	40	n.a.	2667	n.a.	1304	1727	<308	mx	<19	mx	<56	8,7	3,1	<1.5	mx	<13	0,4	17	1,7	<5.3	<1
79	L1	nm02b12		Enargite	L-V	40	n.a.	2758	n.a.	1153	936	149	mx	490	mx	<31	7,8	1,7	<0.8	mx	<6.9	1,4	7,1	<0.4	210	<0.7
80	L1	nm02b13		Enargite	L-V	40	n.a.	2417	n.a.	1319	663	<1881	mx	547	mx	<404	<10.2	<4.6	<9.9	mx	<91	3,0	<18	<5	149	<8.9
81	L1	nm02b15*		Enargite	L-V	75	n.a.	2729	n.a.	1210	1595	<385	mx	81	mx	<86	6,7	2,3	1983	mx	####	3,3	13	10	<7.5	<1.8
82	L1	nm02b16*		Enargite	L-V	40	n.a.	2692	n.a.	1284	1689	<556	mx	<35	mx	<121	8,6	<1.6	1512	mx	####	<0.9	8,5	23	<10	<2.9
83	L1	nm02b18*		Enargite	L-V	30	n.a.	2731	n.a.	1215	1659	<1052	mx	<55	mx	<261	5,0	<2.2	954	mx	7737	1,6	17	<4.8	<16	<3.9
84	L1	nm02b14*		Enargite	L-V	40	n.a.	1563	n.a.	783	686	3529	mx	388	mx	852	4,8	<1.6	<3	mx	79	1,6	11	11	146	584
Late secondary brine inclusions in porphyry vein																									
85	01-B1	dc14j03**		PQ	brine	30	n.a.	94639	mx	45955		####	139	26504	340	n.a.	164	109	9	n.a.	<12	32	n.a.	<0.43	10189	n.a.
86	01-B1	dc14j04**		PQ	brine	30	n.a.	101573	mx	34550		####	113	23176	283	n.a.	131	127	12	n.a.	<21	24	n.a.	<0.16	10715	n.a.

87	01-B1	dc14j05**	PQ	brine	40	n.a.	101142	mx	38610		####	194	19817	262	n.a.	166	63	7	n.a.	<8.9	30	n.a.	<0.11	11812	n.a.
88	01-B1	dc14j06**	PQ	brine	40	n.a.	107724	mx	14265		####	244	30213	330	n.a.	155	54	9	n.a.	<6.5	30	n.a.	<0.08	17146	n.a.
Early pseudosecondary brine inclusions in HS vein																								
89	A-4	ma04b08 08	Quartz-1	brine	22	291	105114	mx	20612	8597	####	337	5946	<48	n.a.	176	10	<6.9	n.a.	<20	20	36,2	<5.7	3760	32
90	A-4	ma04b09 09	Quartz-1	brine	20	210	101035	mx	25022	9246	####	319	6591	138	n.a.	230	13	8	n.a.	<66	27	36,7	<10	4178	34
91	A-4	ma04b10 10	Quartz-1	brine	24	343	102399	mx	25251	9779	####	235	7808	124	n.a.	227	11	14	n.a.	43	26	42,9	<8.7	4189	44
92	A-4	ma04b11 11	Quartz-1	brine	20	206	96803	mx	29036	9695	####	167	16573	80	n.a.	208	17	8	n.a.	12	20	26,4	<3.3	4911	24
Late pseudosecondary aqueous inclusions in HS vein																								
93	A-1	ma04a06 06	Quartz-2	L-V	45	127	2194	mx	852	88	1990	210	53	352	n.a.	<5.7	7	<12	n.a.	<67	<2.3	<9.6	<6.8	<22	<5.3
94	A-1	ma04a07 07	Quartz-2	L-V	40	<193	1869	mx	1241	147	<1618	144	<82	<144	n.a.	13	<5.6	<14	n.a.	<141	2,3	<25	<26	<51	<18
95	A-1	ma04a08 08	Quartz-2	L-V	15	207	2086	mx	916	<52	<670	113	<56	<69	n.a.	5	<4.9	<7.7	n.a.	24	<1.5	<10	1,7	<14	<4.3
96	A-2	ma04a09 09	Quartz-2	L-V	50	192	39449	mx	4242	2158	<1239	102	1888	<103	n.a.	19	<3.7	<9.3	n.a.	<89	7,3	<17	<22	628	<14
97	A-2	ma04a10 10	Quartz-2	L-V	15	<1424	35549	mx	4859	1874	7823	<234	5554	<614	n.a.	<46	13	<161	n.a.	359	6,3	<186	<69	1361	<56
98	A-2	ma04a11 11	Quartz-2	L-V	15	110	50459	mx	3328	825	1324	58	467	<23	n.a.	5	3	<2.8	n.a.	<14	0,6	<6.1	<3.2	326	<2.4
99	A-2	ma04a12 12	Quartz-2	L-V	15	<368	41528	mx	9192	2814	<3759	<179	2075	<314	n.a.	23	<21	<34	n.a.	<171	<7.9	<76	<8.8	685	<24
##	A-3	ma04a13 13	Quartz-2	L-V	18	73	49972	mx	5219	4341	####	61	3525	151	n.a.	81	<1.2	4	n.a.	<22	11,0	17,5	<2.3	1497	33
##	A-3	ma04a14 14	Quartz-2	L-V	22	193	37858	mx	3469	1888	974	<31	1623	<49	n.a.	15	<3.3	<7	n.a.	<50	2,9	<8.9	3,3	419	<3.7
##	A-3	ma04a15 15	Quartz-2	L-V	30	372	35503	mx	8655	2941	1459	<46	1812	<88	n.a.	28	<3.8	<9.7	n.a.	<77	5,3	<25	<13	493	5,8
##	A-3	ma04b05 05	Quartz-2	L-V	40	615	67634	mx	11062	6702	2033	70	6578	<54	n.a.	46	10	62	n.a.	<35	8,3	<13	<4.9	8791	<4.6

Notes: Types of inclusions: brine = three-phase liquid + vapor + halite inclusions; V = vapor; L-V = two-phase liquid-rich. The salinity of trapped in pyrite and enargite fluids used for calculations was 35, 0.5 and 1 wt% NaCl equiv, for the brines, vapor and two-phase inclusions, respectively (see text for explanation). Salinity of quartz-hosted fluid inclusions was calculated from either the halite dissolution temperatures (Sterner et al. 1988) for the brines, or from the temperature of final ice melting (Bodnar 1993) for L-V inclusions.

< value: Concentrations are below the LOD given (3 sigma criterion; Longerich et al., 1996).

* accidentaly trapped solid inclusion of sulfide or telluride

**Analyzed using the "multiple-Au-detection" method of Klemm (2005) aiming to decrease LOD for Au.

Abbreviations: assem. - assemblage; FI - fluid inclusion; HS - high-sulfidation; mx - major element in the host mineral (matrix); n.a. - not analyzed; PQ - quartz from porphyry vein.

Different fluid inclusion assemblages of identical fluid type, trapped in the same host crystal are generally very similar in composition (Fig. 9). The only outliers come from elements interpreted as major constituents of accidentally trapped solid phases, as illustrated in Figure 9a for two pyrite-hosted brine assemblages.

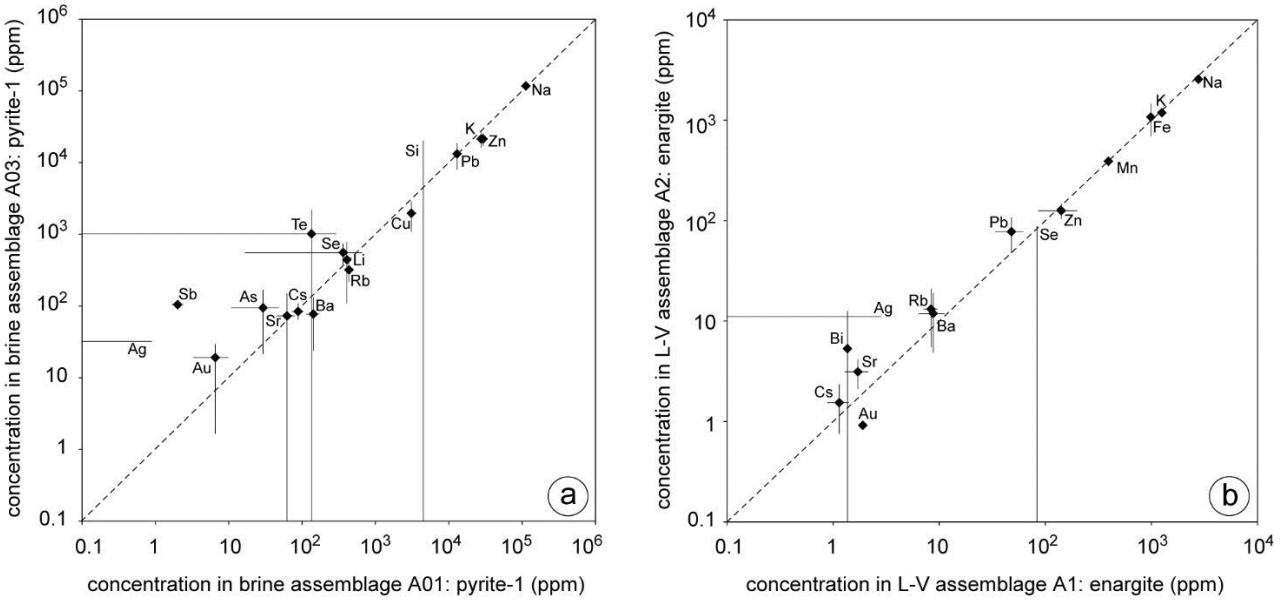

Figure 9. Comparison between element concentrations in two brine fluid inclusion assemblages trapped in *pyrite-1* **(a)** and two liquid-vapor fluid inclusion assemblages trapped in enargite **(b)**. Nearly all the elements have identical concentrations (within their uncertainty) in both pairs of inclusion assemblages, except a few elements such as Te, As, Sb, Au and Ag, enriched in one of the pyrite-hosted assemblages, due to accidentally trapped solid inclusions (see text for discussion). Error bars extending from the bottom of the figure indicate upper limits for analyses where element concentrations are below detection. Error bars show 1σ variability within one assemblage.

Reproducibility data for all elements analyzed in the pyrite-hosted and enargite-hosted fluid inclusion assemblages are illustrated in Figure 10. Commonly the mean relative standard deviation (RSD) values for pyrite-hosted assemblages are 25% or less for Na, K, Rb, Zn, Cs, Pb concentrations (Fig. 10a). RSD values for Sr and Cu are in the range 30-60%. Some metals and semi-metals such as As, Sb, Se, Te, Ag, and Au, whose high concentrations are interpreted to be due to the presence of accidental solid inclusions, have RSD values close to or even higher than 100%. Enargite-hosted fluid inclusion assemblages have systematically lower RSD values than the pyrite-hosted ones (Fig. 10b), most probably due to the larger size of the inclusions. For the major alkalis, Na and K, the RSD is usually below 10%. These data are comparable with previous work conducted on quartz-hosted fluid inclusions (Günther et al., 1998; Heinrich et al., 2003) and could be interpreted as resulting from natural concentration variations. The very good reproducibility of the data for enargite-hosted fluid inclusions of variable size is a good indication that their analysis was not affected by fractionation due to melting of the host mineral during ablation, which would be expected to become more prominent in smaller inclusions.

Figure 11 illustrates the main results of LA-ICP-MS analyses of epithermal fluids at Rosia Poieni. Selected major elements and ore metals are plotted as element/(Na+K) ratios for each group of inclusion assemblages. Element/(Na+K) ratios are relatively accurate and are not dependent on errors generated by absolute salinity estimates of the fluid inclusions (Günther et al., 1998). Some pairs like Ba-Sr or Rb-Cs, i.e., elements whose concentration can largely depend on fluid-rock interaction during feldspar-destructive hydrothermal alteration, show positive correlations (Figs. 11a-b). As Sr- and Ba-bearing minerals are relatively rare in the high-sulfidation epithermal veins (just minor APS minerals and barite are present) the fluid composition would reflect the fluid equilibrium with the host diorite porphyry during its ascent across the potassic and the phyllic alteration zones at Rosia Poieni, and the formation of advanced-argillic alteration at the present level of exposure.

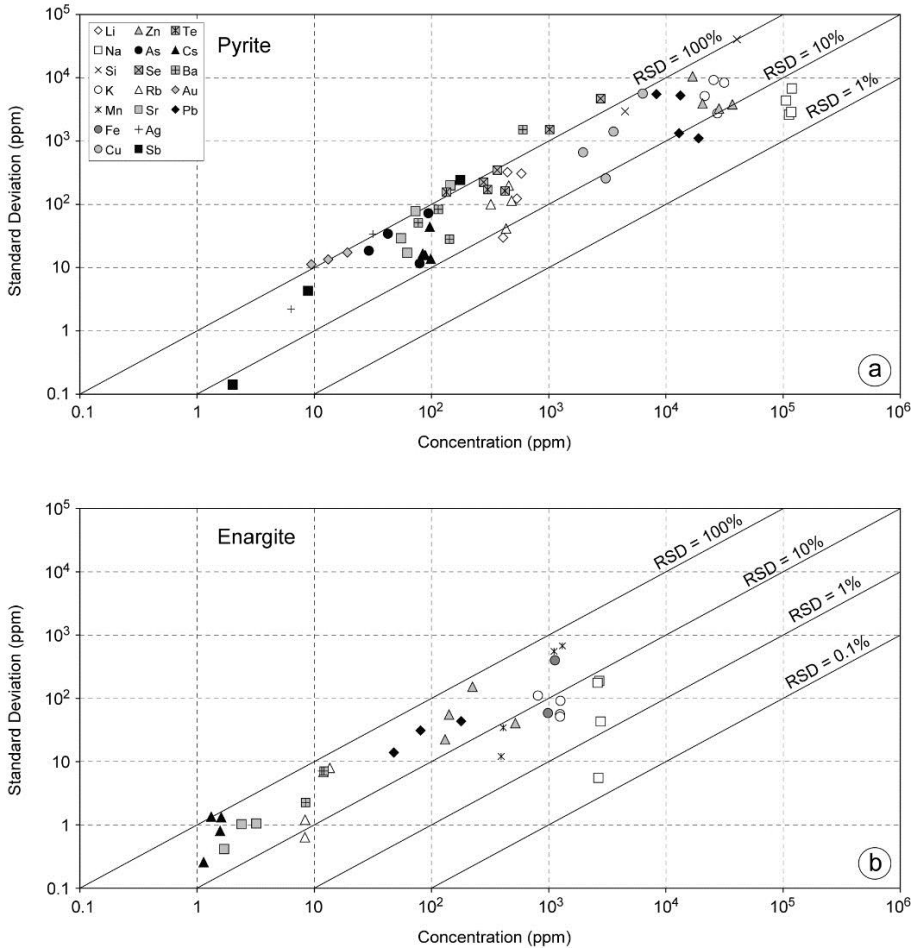

Figure 10. Analytical reproducibility for LA-ICP-MS analysis of fluid inclusions hosted by pyrite **(a)** and enargite **(b)**. Each datapoint represents a relative standard deviation value determined for one element in a fluid inclusion assemblage. Concentrations of elements showing relative standard deviation close to or higher than 100% are due to accidentally trapped solid inclusions.

Texturally all fluid inclusions analyzed in this study belong to the same early-epithermal hydrothermal event at Rosia Poieni. However, our LA-ICP-MS data reveal that the quartz-hosted inclusions have systematically lower Cs/(Na+K) ratios than the pyrite- and enargite-hosted inclusions (Figs. 11b-c) – the extreme difference corresponds to almost one order of magnitude. The quartz-hosted inclusions also have systematically lower Cu content, compared to the pyrite-hosted ones. Just one quartz-hosted fluid inclusion assemblage plots within the trend defined by the sulfide-hosted inclusions on Figure 11c.

Pb/(Na+K) and Zn/(Na+K) display a very good correlation (Fig. 11e), indicative of the common behavior of both elements in the fluids. In absolute concentrations, the Zn:Pb ratio of the epithermal-stage fluids ranges from 1:1 to 6:1. The same Zn/Pb ratio is typical for a wide range of crustal fluid types (Yardley, 2006). The ore metal content of all quartz- and pyrite-hosted individual fluid inclusions is presented on the Cu-Zn-Pb diagram (Fig. 11f). Enargite-hosted fluid inclusions can not be plotted on this diagram, as Cu is a major element in the matrix. Except for three brines and four liquid-vapor inclusions in pyrite (affected by accidentally trapped sulfide/sulfosalt crystals, see below), all fluid inclusions have similar metal proportions. As a rule, the epithermal fluids at Rosia Poieni are depleted in Cu, relative to Zn and Pb, and with higher Zn concentrations than Pb (Fig. 11f; Table 3).

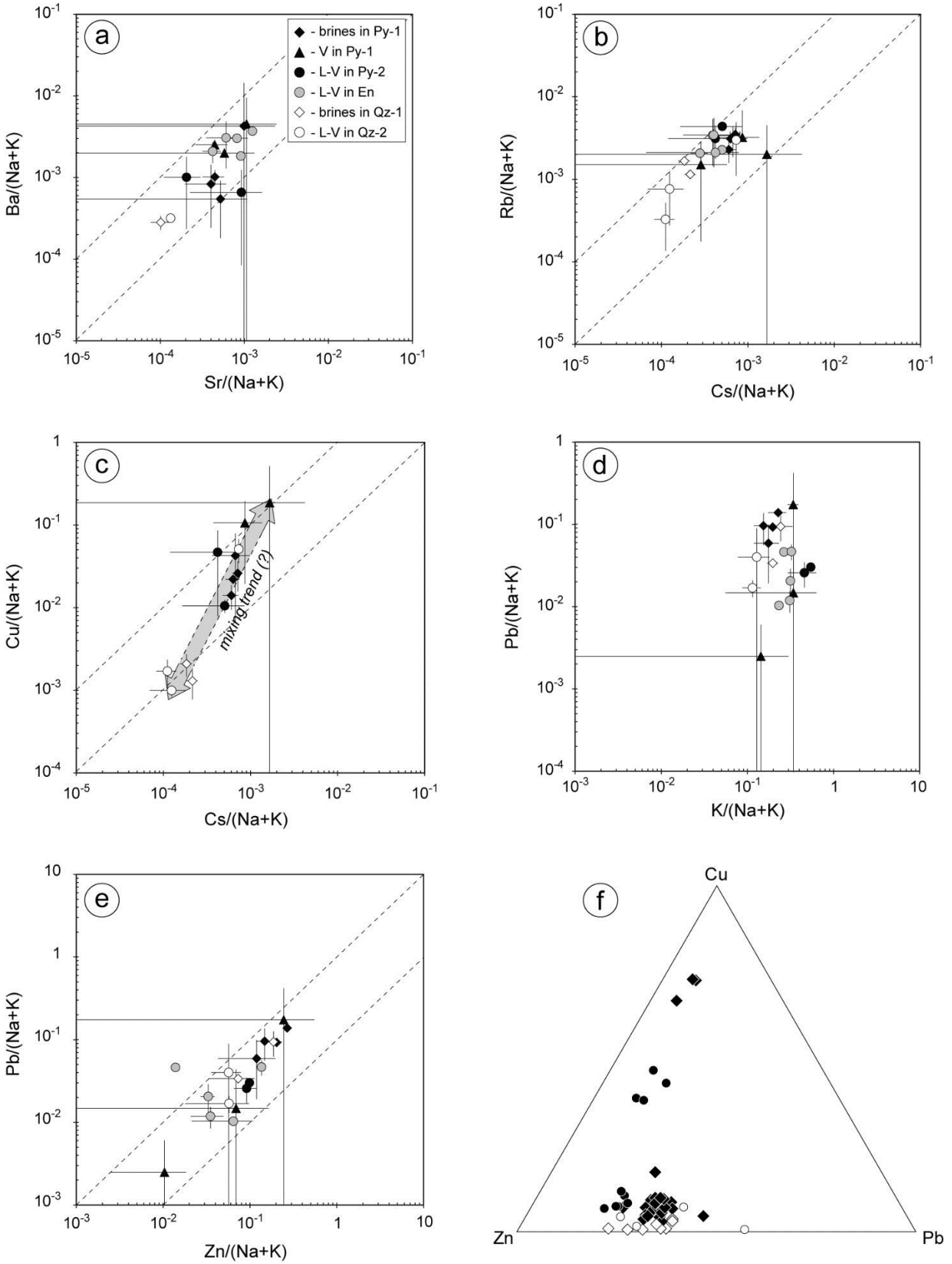

Figure 11. LA-ICP-MS results on fluid inclusion assemblages in epithermal pyrite, enargite and quartz expressed in element/(Na+K) ratios **(a-e)**. Each symbol represents one fluid inclusion assemblage. Error bars indicate 1 of the variability within one assemblage. Dashed lines indicate constant elemental ratios between the elements used in the plot. Figure **11f** is a Zn-Pb-Cu ternary plot of the metal content of epithermal fluids trapped in pyrite and quartz. Each symbol represents a single fluid inclusion. Nearly all measured inclusions show depletion in Cu compared to their Pb and Zn content, due to Cu precipitation in the porphyry environment (as chalcopyrite and bornite) and enargite precipitation in the high-sulfidation epithermal veins.

6.4. Gold in the epithermal fluids at Rosia Poieni

In 43 of the 103 analyzed fluid inclusions, gold was detected in statistically significant quantity (Table 3; Fig. 12a). In more than 50% of these inclusions, Au is present in concentrations between 0.1 and 5 ppm, assuming an uncertainty of 50% for the dilute liquid-vapor and vapor-rich inclusions and 15% for the brine inclusions induced by internal standardization (see discussion in the next chapter). The strong Au affinity for Ag, Sb, As, Te, and Se deduced from time-overlapping peaks in the LA-ICP-MS signals and the correlation between Au and these elements (Figs. 12b-f) can be interpreted as due to heterogeneous trapping of solid inclusions in which gold is present. A similar "nugget effect" for high Au values was recently reported for Au-bearing magmatic quartz-hosted melt inclusions from the Timbarra gold deposit, Australia, also studied by LA-ICP-MS (Mustard et al., 2006) and in hydrothermal fluid inclusions from the Famatina Cu-Mo-Au system, Argentina (Pudack et al., 2006). Considering the suite of elements that correlate positively with Au, we conclude that the trapped microparticles are Ag-Au tellurides or selenides. Such minerals were identified also as microscopic inclusions in pyrite and enargite in the high-sulfidation veins at Rosia Poieni (Fig. 2). The relatively constant concentrations of these elements (within one order of magnitude close to their detection limit) indicate that they were originally present in high concentration in a homogeneous solution and trapped as colloidal-size particles in the inclusions. However, we cannot exclude that they were trapped as separate crystals that had precipitated in open microcracks prior to inclusion healing.

7. Discussion

7.1. LA-ICP-MS analyses of sulfide-hosted fluid inclusions: feasibility and limitations

The combination of NIR petrography and LA-ICP-MS allows quantitative characterization of major- and trace-element contents of single fluid inclusions in well constrained assemblages hosted by ore minerals that are opaque to visible light, and thus to determine directly the composition of ore-precipitating fluids. Analysis of fluid inclusions in ore minerals removes any doubt that the fluids represent the ore-forming fluids, which is not always possible with analysis of fluid inclusions in transparent gangue minerals. In the Rosia Poieni samples we could analyze quartz-hosted fluid inclusions along with pyrite and enargite in well constrained textural relationships, and directly compare their compositions.

The main limitations we were confronted with in this study come from the nature of the host sulfide minerals. First of all, the interaction of the host semiconductor mineral with the incident light in the NIR microscope results in a strong influence of the source light intensity upon the microthermometric measurements. Therefore, microthermometry could not be applied systematically on all of the studied inclusions, leading to estimation (instead of direct measurements) of fluid salinities required as internal standard for the quantification of the LA-ICP-MS data. Precise quantification of element concentrations in dilute fluids (< 5 wt% NaCl salinity) is a common problem, even if salinity measurements are available. Final ice melting temperatures in the H_2O-NaCl system result in an uncertainty of calculated salinity of ± 0.2 wt% NaCl equiv., so that calculated element concentrations have an uncertainty of ± 20% for fluid inclusions with salinity 1 wt% NaCl equiv. This uncertainty is similar in magnitude with the typical laser sampling uncertainty indicated by the external reproducibility in one fluid inclusion assemblage (Heinrich et al., 2003; Pettke, 2008). An uncertainty of 0.5 wt% NaCl on the estimated salinities for the dilute fluids in our vapor-rich and liquid-vapor inclusions translates to an uncertainty of 50% on the calculated element concentrations. For the halite-saturated brines trapped in *pyrite-1*, a maximum uncertainty of 5 wt% NaCl on the estimated salinity would introduce an uncertainty of 15% on the calculated element concentrations. Thus, large uncertainties can be generated by the fluid salinity estimations in some cases even exceeding uncertainties on the external reproducibility of individual inclusions in synthetic or natural fluid inclusion assemblage.

The second limitation is related to the partial melting observed for some sulfide minerals under the laser beam (e.g., Watling et al., 1995; Watling 1998), which seems unavoidable even at low laser energies, despite the short wavelength of the excimer laser. In this study the melting effect was stronger in enargite than in pyrite (Fig. 6). Whenever crystalline sulfide coexists with sulfide melt, there is the possibility that chalcophile elements with very large or very small monosulfide-sulfide melt partition coefficients may fractionate between the phases (Wohlgemuth-Ueberwasser et al., 2007), in addition to the element fractionation due to element partitioning between the residual melt in the ablation pit and

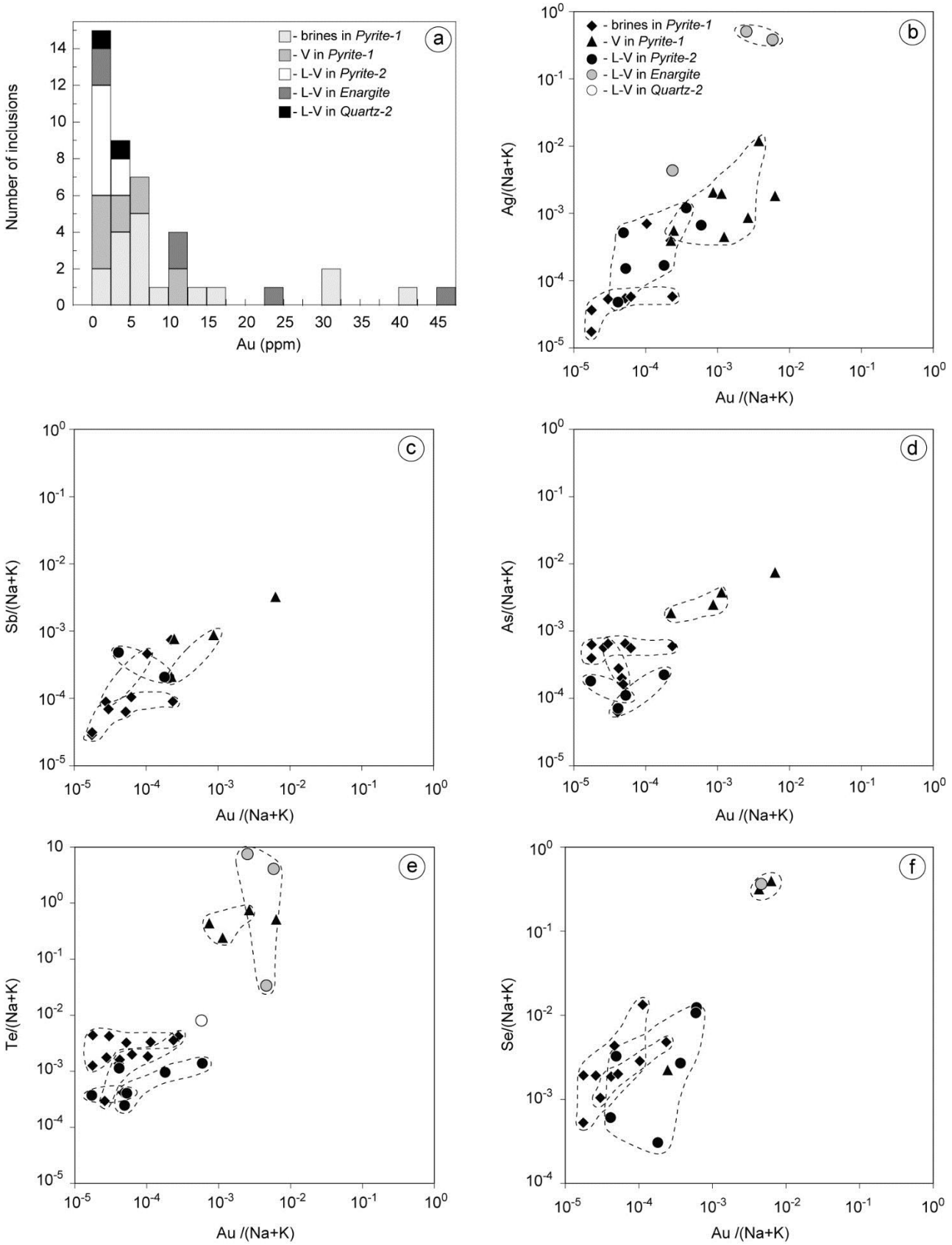

Figure 12. Gold content of pyrite-, enargite-, and quartz-hosted single fluid inclusions from high-sulfidation veins measured by LA-ICP-MS: **a)** Histogram of the gold content of single fluid inclusions; **b-f)** Ag/(Na+K), Sb/(Na+K), As/(Na+K), Te/(Na+K) and Se/(Na+K) vs. Au/(Na+K) plots for single fluid inclusions. Dashed lines group inclusions from the same assemblage.

the vapor plume just above it that is present during the ablation. To minimize laser-induced elemental fractionation, strict matrix matching of external standards and unknowns is commonly employed. However, in this fluid inclusion-oriented LA-ICP-MS study such an approach was impossible, because to our knowledge there is no available sulfide standard enriched in alkalis and thus, the SRM 610 remains the most appropriate external standard for analyses of fluid inclusions, even if they are hosted in a sulfide matrix. In addition, from the very good reproducibility of the data from enargite-hosted fluid inclusions, it seems that the partial melting did not systematically affect the fluid inclusion analyses. Nevertheless, melting during ablation could significantly affect the absolute concentrations of elements in the mineral matrix, which are directly dependent on element intensities; hence, fluid element concentrations with a significant host mineral correction should be interpreted with caution, as well as the quantitative trace element data for sulfides analyzed by using a non-sulfide standard (Sylvester, 2001).

The third limitation for the LA-ICP-MS analysis of sulfide-hosted fluid inclusions is the fact that some ore elements of interest can be major or minor elements in the host sulfide. In the pyrite-hosted inclusions from Rosia Poieni, Fe is a major element in the matrix and therefore was not quantified even though it is probably also a major salt component of the fluids. Elements such as Se and As have very high RSD values, because they are present in the pyrite as trace elements. In enargite, Cu and As (as majors), as well as Sb and Sn (as minor elements) were not quantified in the fluid inclusions. Because all these elements are important ore-metals and their quantification would be of interest, they were systematically analyzed in the quartz-hosted inclusions only.

A minor inconvenience in this study was also the common presence (~40% of the studied inclusions) of tiny (colloidal-size) inclusions of Au-Ag tellurides or selenides, as accidentally trapped solids in the fluid inclusion cavities, as deduced from the trace metal content of the fluid inclusions. Their presence did not affect the results on the alkali concentrations and some metals such as Zn, Pb and Cu, but explains the very common detection of gold (up to ~40 ppm) in the fluid inclusions analyzed.

Quartz- versus sulfide-hosted fluid inclusions and implication for the ore-formation at Rosia Poieni

One of the questions still under debate in fluid inclusion research conducted on hydrothermal ore deposits is: Under what conditions do the fluids in transparent gangue minerals represent the ore-forming fluids, and how can we recognize when these conditions apply? To date, the NIR light microthermometry on fluid inclusions hosted by ore minerals has not provided an unequivocal answer. Several fluid inclusion studies in cogenetic gangue and ore minerals reveal similar homogenization temperatures and salinities of fluid inclusions (e.g., Campbell and Robinson-Cook, 1987; Campbell and Panter, 1990; Lüders et al., 1999; Bailly et al., 2000, 2002), while others report distinct and different salinities for the quartz- and sulfide-hosted fluid inclusions (e.g., Hagemann and Lüders, 2003; Shimizu et al., 2003).

In the present study on the chemistry of texturally similar fluid inclusions in quartz and pyrite/enargite, quartz-hosted fluid inclusion assemblages commonly follow the trends defined by the sulfide-hosted assemblages for most of the elements (Fig. 11a, b, e). However, for some particular elements (Cu and Cs) they have distinctly different compositions (Fig. 11c). In our data set, Cs/(Na+K) ratios of quartz-hosted fluid inclusions are systematically lower, by up to an order of magnitude, than in the sulfide-hosted inclusions. Four out of the five quartz-hosted assemblages form well-defined groups, which coincide with the narrow Cs/(Na+K) range of the porphyry-stage fluids trapped in purple quartz of the stockwork veins. Additionally, the Cu/(Na+K) ratios of these fluids are between one and two orders of magnitude lower compared to the pyrite-hosted inclusions and correspond to some of the lowest Cu/(Na+K) ratios recorded for the porphyry-stage fluids at Rosia Poieni. By contrast, the pyrite-hosted vapor-rich fluid inclusions have the highest Cu/(Na+K) in the trend from Figure 11c, which also corresponds to the highest Cu/(Na+K) ratios found in the porphyry-stage fluid inclusions. Based on the observed textural relationships, *quartz-1* in the high-sulfidation veins at Rosia Poieni predates the sulfide precipitation (Figs. 2, 3a) and our fluid inclusion LA-ICP-MS data suggest that *quartz-1* was formed from a compositionally different fluid as well. Supporting this statement, Figure 13 presents a plot of the composition of one brine assemblage trapped in *quartz-1* versus the composition of one brine assemblage in *pyrite-1*. The pyrite-hosted inclusions show systematically higher concentrations for all elements, except for Na and K which have similar concentrations in both minerals, and As which has always higher concentration in the quartz-hosted inclusions.

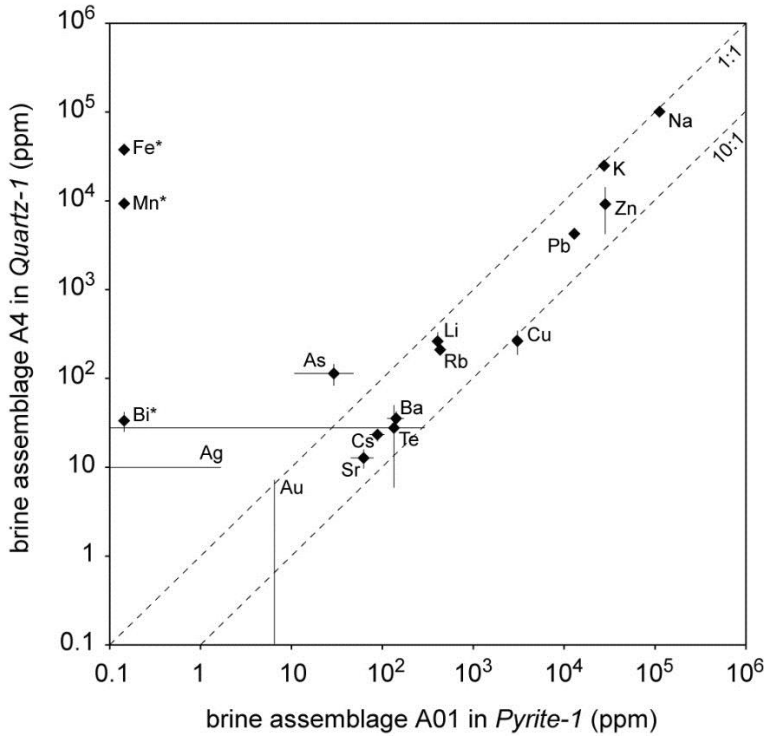

Figure 13. Comparison between element concentrations in two brine fluid inclusion assemblages trapped in *Pyrite-1* and *Quartz-1*. Nearly all elements show higher concentrations in the pyrite-hosted assemblage, except Na and K which have similar concentrations in both assemblages, and As which content is higher in the quartz-hosted assemblage. Elements marked by (*) were measured only in the quartz-hosted inclusions. Error bars indicate 1 of the variability within a single assemblage.

Cesium can be used to monitor the degree of crystallization of the source magma in evolved magmatic-hydrothermal systems (Audétat and Pettke, 2003; Audétat et al., 2008). An increase in ratios of Cs over the sum of major fluid solutes in successive fluid generations have been used previously (Klemm, 2005; Klemm et al., 2008) to argue for different pulses of ore fluid exsolution from residual melt of a progressively crystallizing magma. Such an interpretation, implying different moments of entrapment of different fluid stages, could be also appropriate for the Rosia Poieni system.

Hedenquist et al. (1998) documented the evolution of fluids associated with the porphyry to epithermal transition in the Far Southeast-Lepanto porphyry and epithermal Cu-Au deposits in the Philippines and registered a drastic change in the pressure and temperature regime between the early porphyry and the later epithermal mineralization. Based on their stable isotope study of hydroxyl-bearing alteration minerals associated with epithermal orebodies and fluid inclusion microthermometry of enargite-hosted fluid inclusions (Mancano and Campbell, 1995), they suggested progressive mixing of magmatic fluids with cool ground water with nil salinity. In the present study, the chemical evolution of such fluids at the porphyry to epithermal transition was investigated.

The fluid inclusions trapped in the early generation of epithermal quartz at Rosia Poieni most probably correspond to residual porphyry-stage brines resulting from phase separation that occurred in the porphyry veins as several successive boiling events (Damman et al., 1996). These deep fluids, which lost their Cu content as a result of chalcopyrite/bornite precipitation in stockwork veins at greater depth, were trapped in the shallower epithermal environment, possibly after erosion and collapse of the upper part of the magmatic-hydrothermal system. These fluids mark the very early stage of the porphyry to epithermal transition fluid processes at Rosia Poieni. Mixing with a new pulse of low-salinity magmatic vapor rising from a magma crystallizing at depth could generate the second batch of hydrothermal fluid with higher Cs/(Na+K) ratio from which the sulfides in the high-sulfidation veins precipitated. Thus the fluid inclusions trapped in *quartz-1* and the vapor-rich inclusions trapped in *pyrite-1* correspond to two end-member fluids defining a mixing trend (Fig. 11c). Preliminary stable isotope data on the high-sulfidation veins at Rosia Poieni confirm a dominantly magmatic origin of all stages of mineralizing fluid (Kouzmanov et al., 2007).

Since the Na/K ratio in hydrothermal fluids is mainly controlled by feldspar stability (Orville, 1963), the relatively restricted range of K/(Na+K) measured in the studied epithermal fluids at Rosia Poieni (Fig. 11d) suggests that at the moment of entrapment K-Na exchange between fluid and host rock had

ceased. This result agrees well with the observation that the high-sulfidation epithermal veins at Rosia Poieni were formed as an overprint onto K-alteration or phyllic alteration zones in which the magmatic Na-bearing feldspars have been already replaced by K-bearing hydrothermal minerals, prior to the epithermal event (Kouzmanov et al., 2004; Milu et al., 2004).

8. Conclusions

Detailed mapping of well constrained fluid inclusion assemblages in pyrite and enargite using NIR transmitted/reflected light microscopy allowed LA-ICP-MS analyses of trapped hydrothermal fluids. The major and trace-element compositions of fluid inclusions trapped in sulfide ore minerals opaque to visible light have been determined and compared with texturally similar quartz-hosted fluid inclusions. The results have implications not only for tracing the fluid source processes in the high-sulfidation epithermal veins overprinting the porphyry system at Rosia Poieni, but also for general understanding of the mechanisms of hydrothermal ore-formation. In spite of the first-order textural evidence that the gangue quartz is nearly syngenetic with the ore minerals in the studied veins, distinct fluid compositions record successive pulses of hydrothermal fluids released from progressively more fractionated hydrous magma batches, one of which formed the epithermal mineralization.

Acknowledgements

This study was financed by the Swiss National Science Foundation project 200020-100735. Discussions with and advice from W. Halter, R. Moritz and T. Driesner are appreciated. The journal reviewers Brian Rusk and Andrew Campbell are thanked for constructive comments, which improved the manuscript and Robert Bodnar is thanked for efficient editorial handling. Emilian Rosu, Paul Ivascanu and Emilian Tanasoiu from IGR, and the managements of Gabriel Resources Ltd., Rosia Montana Gold Corporation, and SC Cupru Min SA, Abrud, are thanked for assistance and logistic support in the field.

References

Alderton, D. H. M., and Fallick, A. E., 2000, The nature and genesis of gold-silver-tellurium mineralization in the Metaliferi Mountains of western Romania: Economic Geology, v. 95, p. 495-515.

Allan, M. M., Yardley, B. W. D., Forbes, L. J., Shmulovich, K. I., Banks, D. A., and Shepherd, T. J., 2005, Validation of LA-ICP-MS fluid inclusion analysis with synthetic fluid inclusions: American Mineralogist, v. 90, p. 1767-1775.

André-Mayer, A. S., Leroy, J. L., Marcoux, E., and Lerouge, C., 2001, Inclusions fluides et isotopes du soufre du gisement Cu-Au de Valea Morii (monts Apuseni, Roumanie) : un télescopage porphyre-épithermal neutre?: C. R. Acad. Sci. Paris, Sciences de la Terre et des planètes, v. 333, p. 121-128.

Arribas Jr., A., 1995, Characteristics of high-sulfidation epithermal deposits, and their relation to magmatic fluid, *in* Thompson, J. F. H., ed., Magmas, Fluids, and Ore Deposits, 23. Short Course Series: Victoria, British Columbia, Mineralogical Association of Canada, p. 419-454.

Audétat, A., Günther, D., and Heinrich, C. A., 1998, Formation of a magmatic-hydrothermal ore deposit: Insights with LA-ICP-MS analysis of fluid inclusions: Science, v. 279, p. 2091-2094.

Audétat, A., Günther, D., and Heinrich, C. A., 2000, Magmatic-hydrothermal evolution in a fractionating granite: A microchemical study of the Sn-W-F-mineralized Mole Granite (Australia): Geochimica Et Cosmochimica Acta, v. 64, p. 3373-3393.

Audétat, A., and Pettke, T., 2003, The magmatic-hydrothermal evolution of two barren granites: A melt and fluid inclusion study of the Rito del Medio and Canada Pinabete plutons in northern New Mexico (USA): Geochimica Et Cosmochimica Acta, v. 67, p. 97-121.

Audétat, A., Pettke, T., Heinrich, C. A., and Bodnar, R. J., 2008, The composition of magmatic-hydrothermal fluids in barren and mineralized intrusions: Economic Geology, v. 103, p. 877-908.

Bailly, L., Bouchot, V., Bény, C., and Milési, J.-P., 2000, Fluid inclusion study of stibnite using infrared microscopy; an example from the Brouzils antimony deposit (Vendee, Armorican Massif, France): Economic Geology, v. 95, p. 221-226.

Bailly, L., Grancea, L., and Kouzmanov, K., 2002, Infrared microthermometry and chemistry of wolframite from the Baia Sprie epithermal deposit, Romania: Economic Geology, v. 97, p. 415-423.

Bodnar, R. J., 1993, Revised equation and table for determining the freezing point depression of H_2O-NaCl solutions: Geochimica et Cosmochimica Acta, v. 57, p. 683-684.

Bostinescu, S., 1984, Porphyry copper systems in the South Apuseni Mountains, Romania.: Annuaire de l'Institut de Géologie et Géophysique, v. 64, p. 163-174.

Campbell, A., Robinson-Cook, S., and Amindyas, C., 1988, Observation of fluid inclusions in wolframite from Panasqueira, Portugal: Bulletin de Minéralogie, v. 111, p. 251-256.

Campbell, A. R., Hackbarth, C. J., Plumlee, G. S., and Petersen, U., 1984, Internal features of ore minerals seen with the infrared microscope: Economic Geology, v. 79, p. 1387-1392.

Campbell, A. R., and Panter, K. S., 1990, Comparison of fluid inclusions in coexisting (cogenetic?) wolframite, cassiterite, and quartz from St. Michael's Mount and Cligga Head, Cornwall, England, *in* Bodnar Robert, J., ed., Current research on fluid inclusions., 54; 3. Geochimica et Cosmochimica Acta: Oxford, International, Pergamon, p. 673-681.

Campbell, A. R., and Robinson-Cook, S., 1987, Infrared fluid inclusion microthermometry on coexisting wolframite and quartz: Economic Geology, v. 82, p. 1640-1645.

Ciobanu, C. L., Gabudeanu, B., and Cook, N. J., 2004, Neogene ore deposits and metallogeny of the Golden Quadrilateral, South Apuseni Mts., Romania, *in* Cook, N. J., and Ciobanu, C. L., eds., Au-Ag-telluride Deposits of the Golden Quadrilateral, Apuseni Mts., Romania. Guidebook of the International Field Workshop of IGCP project 486, Alba Iulia, Romania, 31 August - 7 September 2004, IAGOD Guidebook Series 12, p. 23-88.

Czamanske, G. K., Roedder, E., and Burns, F. C., 1963, Neutron activation analysis of fluid inclusions for copper, manganese, and zinc: Science, v. 140, p. 401-403.

Damman, A. H., Kars, S. M., Touret, J. L. R., Rieffe, E. C., Kramer, J., Vis, R. D., and Pintea, I., 1996, PIXE and SEM analyses of fluid inclusions in quartz crystals from the K-alteration zone of the Rosia Poieni porphyry-Cu deposit, Apuseni mountains, Romania: European Journal of Mineralogy, v. 8, p. 1081-1096.

Einaudi, M. T., Hedenquist, J. W., and Inan, E. E., 2003, Sulfidation state of fluids in active and extinct hydrothermal systems: Transitions from porphyry to epithermal environments: SEG Special Publication, v. 10, p. 285-313.

Günther, D., Audétat, A., Frischknecht, R., and Heinrich, C. A., 1998, Quantitative analysis of major, minor and trace elements in fluid inclusions using laser ablation inductively coupled plasma mass spectrometry: Journal of Analytical Atomic Spectrometry, v. 13, p. 263-270.

Günther, D., Frischknecht, R., Heinrich, C. A., and Kahlert, H. J., 1997, Capabilities of an Argon Fluoride 193 nm excimer laser for laser ablation inductively coupled plasma mass spectrometry microanalysis of geological materials: Journal of Analytical Atomic Spectrometry, v. 12, p. 939-944.

Hagemann, S. G., and Lüders, V., 2003, P-T-X conditions of hydrothermal fluids and precipitation mechanism of stibnite-gold mineralization at the Wiluna lode-gold deposits, Western Australia: conventional and infrared microthermometric constraints: Mineralium Deposita, v. 38, p. 936-952.

Hedenquist, J. W., Arribas, A., and Reynolds, T. J., 1998, Evolution of an intrusion-centered hydrothermal system: Far Southeast-Lepanto porphyry and epithermal Cu-Au deposits, Philippines: Economic Geology, v. 93, p. 373-404.

Heinrich, C. A., Pettke, T., Halter, W. E., Aigner-Torres, M., Audétat, A., Günther, D., Hattendorf, B., Bleiner, D., Guillong, M., and Horn, I., 2003, Quantitative multi-element analysis of minerals, fluid and melt inclusions by laser-ablation inductively-coupled-plasma mass- spectrometry: Geochimica Et Cosmochimica Acta, v. 67, p. 3473-3497.

Henley, R. W., 1985, The geothermal framework of epithermal deposits, *in* Berger, B. R., and Bethke, P. M., eds., Geology and geochemistry of epithermal systems., 2. Reviews in Economic Geology: Socorro, NM, United States, Society of Economic Geologists, p. 1-24.

Klemm, L. M., 2005, Cu-Mo-Au ratios in porphyry-type ore deposits: Constraints from fluid inclusion microanalysis: Unpub. PhD thesis, ETH-Zurich, 162 p.

Klemm, L. M., Pettke, T., Heinbicth, C. A., and Campos, E., 2007, Hydrothermal evolution of the El Teniente deposit, Chile: Porphyry Cu-Mo ore deposition from low-salinity magmatic fluids: Economic Geology, v. 102, p. 1021-1045.

Klemm, L. M., Pettke, T., and Heinrich, C. A., 2008, Fluid and source magma evolution of the Questa porphyry Mo deposit, New Mexico, USA.: Mineralium Deposita, v. 43, p. 533-552.

Kouzmanov, K., Bailly, L., Ramboz, C., Rouer, O., and Beny, J. M., 2002, Morphology, origin and infrared microthermometry of fluid inclusions in pyrite from the Radka epithermal copper deposit, Srednogorie zone, Bulgaria: Mineralium Deposita, v. 37, p. 599-613.

Kouzmanov, K., Ivascanu, P., and O'Connor, G., 2005a, Porphyry Cu-Au and epithermal Au-Ag deposits in the southern Apuseni Mountains, Romania - South Apuseni Mountains district: Lat. 46 degrees 03 ' N, Long. 22 degrees 58 ' E: Ore Geology Reviews, v. 27, p. 46-47.

Kouzmanov, K., Vennemann, T., Putlitz, B., Baumgartner, L., Skora, S., and Heinrich, C. A., 2007, Magmatic fluids in high-sulfidation epithermal veins overprinting a porphyry copper system: Stable isotope study of pyrite-hosted fluid inclusions: European Current Research on Fluid Inclusions (ECROFI-XIX), University of Bern, Switzerland, 17-20 July, 2007, Abstract Volume, 2007, p. 114.

Kouzmanov, K., von Quadt, A., Peytcheva, I., Harris, C., Heinrich, C. A., Rosu, E., and O'Connor, G., 2005b, Rosia Poieni porphyry Cu-Au and Rosia Montana epithermal Au-Ag deposits, Apuseni Mts, Romania: Timing of magmatism and related mineralisation., *in* Cook, N. J., and Bonev, I. K., eds., Au-Ag-Te-Se deposits, IGCP Project 486 - Proceedings of the 2005 Field Workshop, Kiten, Bulgaria, 14-19 September 2005, p. 113-117.

Kouzmanov, K., Wallier, S., Rey, R., Pettke, T., Ivascanu, P. M., and Heinrich, C. A., 2004, Fluid processes at the porphyry-to-epithermal transition: Rosia Poieni copper-gold deposit, Romania., *in* Muhling, J., Goldfarb, R., Vielreicher, N., Bierlein, F., Stumpfl, E., Groves, D. I., and Kenworth, S., eds., Predictive Mineral Discovery Under Cover - Proceedings of the SEG 2004 Conference, Perth, Western Australia, 27 September - 1 October 2004: Perth, Western Australia, p. 383-386.

Kulis, J., and Campbell, A., 1999, Cobalt control on near-infrared transparency of pyrite., *in* Abstracts with Programs - Geological Society of America, v. 31 (7), p. 170.

Landtwing, M. R., Pettke, T., Halter, W. E., Heinrich, C. A., Redmond, P. B., Einaudi, M. T., and Kunze, K., 2005, Copper deposition during quartz dissolution by cooling magmatic-hydrothermal fluids: The Bingham porphyry: Earth and Planetary Science Letters, v. 235, p. 229-243.

Lindaas, S. E., Kulis, J., and Campbell, A. R., 2002, Near-infrared observation and microthermometry of pyrite-hosted fluid inclusions: Economic Geology, v. 97, p. 603-618.

Longerich, H. P., Jackson, S. E., and Günther, D., 1996, Laser ablation inductively coupled plasma mass spectrometric transient signal data acquisition and analyte concentration calculation: Journal of Analytical Atomic Spectrometry, v. 11, p. 899-904.

Loucks, R. R., and Mavrogenes, J. A., 1999, Gold solubility in supercritical hydrothermal brines measured in synthetic fluid inclusions: Science, v. 284, p. 2159-2163.

Lüders, V., 1996, Contribution of infrared microscopy to fluid inclusion studies in some opaque minerals (wolframite, stibnite, bournonite): Metallogenic implications: Economic Geology, v. 91, p. 1462-1468.

Lüders, V., Gutzmer, J., and Beukes, N. J., 1999, Fluid inclusion studies in cogenetic hematite, hausmannite, and gangue minerals from high-grade manganese ores in the Kalahari manganese field, South Africa: Economic Geology, v. 94, p. 589-596.

Lüders, V., and Ziemann, M., 1999, Possibilities and limits of infrared light microthermometry applied to studies of pyrite-hosted fluid inclusions: Chemical Geology, v. 154, p. 169-178.

Mancano, D. P., and Campbell, A. R., 1995, Microthermometry of enargite-hosted fluid inclusions from the Lepanto, Philippines, high-sulfidation Cu-Au deposit: Geochimica et Cosmochimica Acta, v. 59, p. 3909-3916.

Manske, S. L., Hedenquist, J. W., O'Connor, G., Tamas, C., Cauuet, B., Leary, S., and Minut, A., 2006, Rosia Montana, Romania: Europe's largest gold deposit: SEG Newsletter, v. 64, p. 1, 9-15.

Milu, V., Milési, J. P., and Leroy, J. L., 2004, Rosia Poieni copper deposit, Apuseni Mountains, Romania: advanced argillic overprint of a porphyry system: Mineralium Deposita, v. 39, p. 173-188.

Moritz, R., 2006, Fluid salinities obtained by infrared microthermometry of opaque minerals: Implications for ore deposit modeling - A note of caution: Journal of Geochemical Exploration, v. 89, p. 284-287.

Mustard, R., Ulrich, T., Kamenetsky, V. S., and Mernagh, T., 2006, Gold and metal enrichment in natural granitic melts during fractional crystallization: Geology, v. 34, p. 85-88.

Nedelcu, L., Rosu, E., and Costea, C., 2001, Mineral microinclusions hosted in sulfides of main Neogene porphyry copper and epithermal ore deposits of the South Apuseni Mountains, Romania: ABCD-GEODE 2001 Workshop, 8-12 June 2001, Vata Bai, Romania. Abstracts volume., Vata Bai, Romania, 2001, Romanian Journal of Mineral Deposits, p. 72-73.

Orville, P. M., 1963, Alkali Ion Exchange between Vapor and Feldspar Phases: American Journal of Science, v. 261, p. 201-237.

Pačevski, A., Libowitzky, E, Živković, P., Dimitrijević, R, and Cvetković, L., 2008, Copper-bearing pyrite from the Coka Marin polymetallic deposit, Serbia: mineral inclusions or true solid-solution?: Canadian Mineralogist, v. 46, p.249-261.

Pettke T., 2008, Analytical protocols for element concentration and isotope ratio measurements in fluid inclusions by LA-(MC)-ICP-MS. *in*: Sylvester, P., (ed) Laser ablation ICP-MS in the Earth Sciences: Current practices and outstanding issues - Mineral. Assoc. Can. Short Course Series Volume 40, p. 189-218.

Pettke, T., Halter, W., MacIntosh, I., and Heinrich, C. A., 2001, The porphyry to epithermal link: Preliminary fluid chemical results from Rosia Poieni, Romania, and Famatina, Argentina, 2001.

Pudack, C., Halter, W., Heinrich, C. A., and Pettke, T., 2006, The potential role of vapor contraction in the formation of the HS-epithermal Au-Te-As-Cu system at Famatina, Argentina. : Society of Economic Geologists (SEG) Conference, Keystone, Colorado, USA, May 13-16 (poster abstract). 2006.

Redmond, P. B., Einaudi, M. T., Inan, E. E., Landtwing, M. R., and Heinrich, C. A., 2004, Copper deposition by fluid cooling in intrusion-centered systems: New insights from the Bingham porphyry ore deposit, Utah: Geology, v. 32, p. 217-220.

Richards, J. P., and Kerrich, R., 1993, Observations of zoning and fluid inclusions in pyrite using a transmitted infrared light microscope (l < 1.9 μm): Economic Geology, v. 88, p. 716-723.

Roedder, E., 1958, Technique for extraction and partial chemical analysis of fluid-filled inclusions from minerals: Economic Geology, v. 53, p. 235-269.

Roedder, E., 1962, Studies of fluid inclusions I: Low temperature application of a dual-purpose freezing and heating stage: Economic Geology, v. 57, p. 1045-1061.

Roedder, E., 1963, Studies of fluid inclusions II: Freezing data and their interpretation: Economic Geology, v. 58, p. 167-211.

Roedder, E., 1984, Fluid inclusions. Reviews in Mineralogy, v. 12, Mineralogical Society of America, 646 p.

Roedder, E., Ingram, B., and Wayne, E. H., 1963, Studies of fluid inclusions III: Extraction and quantitative analysis of inclusions in the miligram range: Economic Geology, v. 58, p. 353-374.

Rosu, E., Seghedi, I., Downes, H., Alderton, D. H. M., Szakacs, A., Pecskay, Z., Panaiotu, C., Panaiotu, C. E., and Nedelcu, L., 2004, Extension-related Miocene calc-alkaline magmatism in the Apuseni Mountains, Romania: Origin of magmas: Schweizerische Mineralogische Und Petrographische Mitteilungen, v. 84, p. 153-172.

Rusk, B., and Reed, M., 2002, Scanning electron microscope-cathodoluminescence analysis of quartz reveals complex growth histories in veins from the Butte porphyry copper deposit, Montana: Geology, v. 30, p. 727-730.

Rusk, B. G., Reed, M. H., Dilles, J. H., Klemm, L. M., and Heinrich, C. A., 2004, Compositions of magmatic hydrothermal fluids determined by LA- ICP-MS of fluid inclusions from the porphyry copper-molybdenum deposit at Butte, MT: Chemical Geology, v. 210, p. 173-199.

Shimizu, T., Aoki, M., and Kabashima, T., 2003, Near-infrared and visible light microthermometry of fluid inclusions in sphalerite from a possible southeast extension of the Toyoha polymetallic deposit, Japan: Resource Geology, v. 53, p. 115-126.

Sillitoe, R. H., and Hedenquist, J. W., 2003, Linkages between volcanotectonic settings, ore-fluid compositions, and epithermal precious metal deposits: SEG Special Publication, v. 10, p. 315-343.

Sterner, S. M., and Bodnar, R. J., 1984, Synthetic fluid inclusions in natural quartz. I. Compositional types synthesized and applications to experimental geochemistry: Geochimica et Cosmochimica Acta, v. 48, p. 2659-2668.

Sterner, S. M., Hall, D. L., and Bodnar, R. J., 1988, Synthetic fluid Inclusions. 4. Solubility relations in the system NaCl-KCl-H_2O under vapor-saturated conditions: Geochimica et Cosmochimica Acta, v. 52, p. 989-1005.

Stoffell, B., Appold, M.S., Wilkinson, J.J., McClean, N.A., Jeffries, T.E., 2008, Geochemistry and evolution of Mississippi valley-Type mineralizing brines from the tri-State and Northern Arkansas Districts determined by LA-ICP-MS microanalysis of fluid inclusions: Economic Geology, v. 103, p. 1411-1435.

Sylvester, P., 2001, A Practical Guide to Platinum-Group Element Analysis of sulfides by Laser-Ablation ICPMS, *in* Sylvester, P., ed., Laser-Ablation-ICPMS in the Earth Sciences: Newfoundland, Mineralogical Association of Canada, Short Course Series, v. 29, p. 203-211.

Udubasa, G., Rosu, E., Seghedi, I., and Ivascanu, P. M., 2001, The "Golden quadrangle" in the Metaliferi Mts, Romania: What does really mean?, *in* Udubasa, G., Veliciu, S., Berza, T., Maruntiu, M., Popescu, G.,

Paul, C., Rosu, E., Sandulescu, M., and Stelea, I., eds., ABCD-GEODE 2001 Workshop Vata Bai, Romania. Abstracts volume, Romanian Journal of Mineral Deposits: Bucharest, Romania, Geological Institute of Romania, vol. 79 (2), p. 24-34.

Ulrich, T., Günther, D., and Heinrich, C. A., 2001, The evolution of a porphyry Cu-Au deposit, based on LA-ICP-MS analysis of fluid inclusions: Bajo de la Alumbrera, Argentina: Economic Geology, v. 96, p. 1743-1774.

Wallier, S., Rey, R., Kouzmanov, K., Pettke, T., Heinrich, C. A., Leary, S., O'Connor, G., Tamas, C. G., Vennemann, T., and Ullrich, T., 2006, Magmatic fluids in the breccia-hosted epithermal Au-Ag deposit of Rosia Montana, Romania: Economic Geology, v. 101, p. 923-954.

Watling, R. J., 1998, In-line mass transport measurement cell for improving quantification in sulfide mineral analysis using laser ablation inductively coupled plasma mass spectrometry: Journal of Analytical Atomic Spectrometry, v. 13, p. 927-934.

Watling, R. J., Herbert, H. K., and Abell, I. D., 1995, The Application of Laser Ablation-Inductively Coupled Plasma-Mass Spectrometry (LA-ICP-MS) to the Analysis of Selected Sulfide Minerals: Chemical Geology, v. 124, p. 67-81.

Wilkinson, J. J., Boyce, A. J., Earls, G., and Fallick, A. E., 1999, Gold remobilization by low-temperature brines: Evidence from the Curraghinalt gold deposit, northern Ireland: Economic Geology, v. 94, p. 289-296.

Wilkinson, J. J., Stoffell, B., Wilkinson, C. C., JEFFRIES, T., E., and Appold, M. S., 2009, Anomalously metal-rich fluids form hydrothermal ore deposits: Science, v. 323, p. 764-767.

Wohlgemuth-Ueberwasser, C. C., Ballhaus, C., Berndt, J., Paliulionyte, V. S. N., and Meisel, T., 2007, Synthesis of PGE sulfide standards for laser ablation inductively coupled plasma mass spectrometry (LA-ICP-MS): Contributions to Mineralogy and Petrology, v. 154, p. 607-617.